Dynamical Passage to Approximate Equilibrium Shapes for Spinning, Gravitating Rubble Asteroids

Ishan Sharma *

Department of Mechanical Engineering, IIT Kanpur, Kanpur 208016, India.

James T. Jenkins Joseph A. Burns **

Department of Theoretical and Applied Mechanics
Cornell University, Ithaca, NY 14853

Abstract

Many asteroids are thought to be particle aggregates held together principally by self-gravity. Here we study–for static and dynamical situations– the equilibrium shapes of spinning asteroids that are permitted for rubble piles. As in the case of spinning fluid masses, not all shapes are compatible with a granular rheology. We take the asteroid to always be an ellipsoid with an interior modeled as a rigid-plastic, cohesion-less material with a Drucker-Prager yield criterion. Using an approximate volume-averaged procedure, based on the classical method of moments, we investigate the dynamical process by which such objects may achieve equilibrium. We first collapse our dynamical approach to its statical limit to derive regions in spin-shape parameter space that allow equilibrium solutions to exist. At present, only a graphical illustration of these solutions for a prolate ellipsoid following the Drucker-Prager failure law is available (Sharma et al. *BAAS* 37 [2005a], 643; Sharma et al. *Proceedings of the 5th International Conference on Micromechanics of Granular Media* Vol. 1 [2005b], 429; Holsapple, *Icarus* **154** [2006], 500). Here, we obtain the equilibrium landscapes for general triaxial ellipsoids, as well as provide the requisite governing formulae. In addition, we demonstrate that it may be possible to better interpret the results of Richardson et al. (2005) (*Icarus* **173** [2004], 349) within the context of a Drucker-Prager material. The graphical result for prolate ellipsoids in the static limit is the same as those of Holsapple (*Icarus* **154** [2006], 500) because, when worked out, his final equations will match ours. This is because, though the formalisms to reach these expressions differ, in *statics*, at the *lowest level of approximation*, volume-averaging and the approach of Holsapple (*Icarus* **154** [2006], 500) coincide.

We note that the approach applied here was obtained independently (*BAAS* 35 [2003], 1034; Sharma, Cornell University dissertation, 2004); it provides a general, though approximate, framework that is amenable to systematic improvements and

is flexible enough to incorporate the dynamical effects of a changing shape, different rheologies and complex rotational histories. To demonstrate our technique, we investigate the non-equilibrium dynamics of rigid-plastic, spinning, prolate asteroids to examine the simultaneous histories of shape and spin rate for rubble piles. We have succeeded in recovering most results of Richardson et al. (*Icarus* **173** [2004], 349), who obtained equilibrium shapes by studying numerically the passage into equilibrium of aggregates containing discrete, interacting, frictionless, spherical particles. Our mainly analytical approach aids in understanding and quantifying previous numerical simulations.

---

1 Introduction

Investigations of spinning fluid masses begin with Newton who, assuming a small asphericity, determined the Earth's flattening. Later, Maclaurin calculated the equilibrium shapes of oblate fluid rotators - the eponymous Maclaurin spheroids - and further showed that prolate equilibrium shapes cannot be obtained. Truly triaxial ellipsoidal shapes of equilibrium for spinning fluids were thought to be unrealizable until Jacobi provided an argument in support of their existence. These so-called Jacobi ellipsoids branch off from the Maclaurin sequence. Flatter (lower aspect ratio) oblate Maclaurin ellipsoids spinning about their maximum inertia axis become unstable, and begin the Jacobian sequence of stable "equilibrium" triaxial ellipsoids. The equilibrium shapes of spinning fluid ellipsoids are covered comprehensively by Chandrasekhar (1969) in a unified manner, using the volume-averaged method outlined below in Sec. 2.

Recent research (Richardson et al. 2002) has suggested that asteroids are incoherent structures held together by self-gravity and best modeled as granular aggregates, more colloquially known as 'rubble piles'. Observations also show that the vast majority of asteroids are in a state of pure spin about their axes of maximum inertia. This motivates us to study the equilibrium shapes of spinning aggregates taken to be ellipsoids as a first approximation. Like fluids, granular materials place restrictions, though not as severe, on the allowable shapes of spinning ellipsoids by limiting the amount of stress that can be tolerated. Such restrictions may help constrain the internal properties of asteroids and, thus, may constitute a first step towards solving the inverse problem of inferring the asteroids' interiors from a knowledge of their shapes

---

* Previously at the Department of Theoretical and Applied Mechanics, Cornell University, Ithaca, NY 14853.
**Also at the Department of Astronomy, Cornell University.
    Email address: ishans@iitk.ac.in (Ishan Sharma).

and spins. This is especially important now that the shape and spin states of many asteroids are known accurately, either from radar observations (Ostro et al. 2002) or by inverting light curve data (Pravec et al. 2002).

Granular materials display a wide range of behavior, from nearly rigid structures to loose fluid-like flows. If asteroids are indeed gravitationally held rubble piles, it seems appropriate to consider them as dense frictional aggregates modeled as a rigid-plastic material obeying a pressure-dependent yield criterion. Holsapple (2001), when considering equilibrium shapes, used one such rheology for asteroid interiors. In particular, his bodies were elastic-plastic and obeyed a Mohr-Coulomb yield criterion. But, because he did not address deformation due to elasticity, and because his boundary conditions were phrased directly in terms of external forces without recourse to displacements, elastic constants do not enter into his analysis [1]. Thus, we do not lose information by assuming rigid-plasticity in the present analysis. Holsapple's (2001) investigation relied on techniques of limit analysis from plasticity theory (Chen and Han 1987). In particular, he employed the lower limit theorem, which states that, if a stress field that satisfies the boundary conditions and the linear-momentum balance equations can be found, and if that stress field does not violate the yield condition at any point in the body, then the body will not fail. Such a stress field is called a *statically admissible* stress field. Note that failure in the context of the lower limit theorem refers to a failure of the body as a whole (*global failure*), and *not* just to *localized yield* as is often the product of most elastic analyses. It is entirely possible that a body may yield locally in several places but still remain intact. An immediate example is a sphere with a pressurized cavity. As the pressure grows, the inner part of the sphere yields, but the sphere as a whole is kept in place by the outer undamaged material.

Holsapple (2001) was able to find a stress field that was both admissible and *unique* at the time of failure. It was unique in that it could be shown that any smaller admissible stress field could not exist. Hence, the stress field used by Holsapple (2001) was also a *limiting* stress field, so that when this stress field predicted failure, the elastic-plastic body had to fail. The converse that a failing body would require that Holsapple's (2001) stress field to also predict failure is not necessarily true. Using this limiting stress field, Holsapple (2001) was able to map out regions in spin-shape space where ellipsoids could exist in equilibrium. In contrast to the above approach, the volume-averaged approach presented below seeks loadings that initiate yield. However, it is important to remember that because we work with volume averages, we in fact look for incipient yield on the average, a much stronger requirement than the corresponding local one. It is stronger in the sense that while an object

---

[1] The stress field must satisfy boundary conditions. If these involve displacements, the appropriate connections between stresses and displacements has to be made via a constitutive assumption, say, elasticity.

that has yielded on average must necessarily have yielded somewhere locally, the converse is not true. Thus, conditions that guarantee yielding on average will most certainly have initiated local yield in the body. In fact, it will be seen that for the problem at hand, yielding on average will coincide with global failure. Because of this, we will employ the terms "yield" and "failure" interchangeably when discussing our volume-averaged results.

Later, Holsapple (2002) and Holsapple (2004) presented an alternate way to recover the results of Holsapple (2001). This technique employed the *static* version of Signorini's theory of stress means (Truesdell and Toupin 1960, p. 574), which yields the same equations as ours, but only under certain *special* conditions. Specifically, our volume-averaged approach, which is an extension of Chandrasekhar's (1969) virial method to solid bodies, is a scheme of systematic approximation to the balance of momentum that results in *dynamical* equations that at *lowest order*, and in *statics*, are those of Holsapple's (2004) method. By "dynamical" we refer to the presence of strain rates in our governing equations, while "statics" indicates that in neglecting deformations, the equations are restricted to only non-deforming bodies. The methodology in this paper, in contrast to Holsapple (2004), includes the dynamical effects of a deforming shape, and can be extended to investigate dynamical situations of greater complexity involving, perhaps, rheologies more natural to modeling granular media. This flexibility of the present approach has been independently demonstrated earlier in the context of the Earth's Chandler wobble (Sharma et al. 2003 and Sharma 2004), equilibrium shapes of asteroids in steady spins (Sharma 2004, Sharma et al. 2005a, 2005b), the Roche limit for rubble piles (Sharma et al. 2005a and Sharma et al. 2006) and planetary flybys (Sharma 2004 and Sharma et al. 2006). It will also be apparent in the following sections.

Richardson et al. (2005) used an N-body code to study the equilibrium shapes of spinning dense granular aggregates, modelling them as collections of identical smooth spheres held together by their gravity alone. From an initial (non-equilibrium) configuration the evolution of each sphere was followed using a discrete element code until equilibrium was attained.

Here we investigate the failure of asteroids modeled as rubble ellipsoids in pure spin using a volume-averaged method. We first obtain regions in parameter space describing the shape where, for a given spin, an ellipsoidal asteroid can exist. We next apply it to the study of the *dynamical* evolution of a non-equilibrium (deforming) ellipsoid. Not only does the latter exercise establish the strength of our approach, it also helps us to evaluate the appropriateness of comparing a continuum approach to the discrete model used by Richardson et al. (2005), with the additional benefit of quantifying the observations of Richardson et al. (2005).

4

Throughout, we invoke the Drucker-Prager yield criterion (see Sec. 2.1). This yield criterion serves as a smooth outer envelope to the Mohr-Coulomb law utilized by Holsapple (2004). The Drucker-Prager criterion was first employed for investigating spinning rubble piles by Sharma (2004) and Sharma et al. (2005b). Recently Holsapple (2007), following Holsapple's (2004) methodology, also used the Drucker-Prager law to probe the effect of cohesion on the allowed equilibrium shapes of a proloidal rotator. At present, however, there is available only a graphical specification of a prolate Ducker-Prager ellipsoid's equilibrium landscape with no supporting equations. Within we close this gap by providing a complete description of these allowed equilibrium shapes for general triaxial ellipsoids using the Drucker-Prager yield criterion.

An investigation of the equilibrium shapes with a Drucker-Prager yield criterion serves many purposes. First, constitutive models based on Drucker-Prager and Mohr-Coulomb yield criteria are the two most commonly invoked for geophysical materials. So, a detailed comparison between the predictions of these two yield criteria may well be profitable. Next, being smoother, the Drucker-Prager criterion alleviates complications introduced by sharp edges present in the Mohr-Coulomb yield surface. For this reason, we utilize the Ducker-Prager law when investigating the dynamics of a spinning rubble pile. Thus, a study of the static equilibrium landscape serves as a point of departure for the more involved dynamical exploration that follows. Third, we will see that the Drucker-Prager criterion may be better suited to interpret the computational results of Richardson et al. (2005). Finally, as is clear from the previous discussion, our method and that followed by Holsapple (2004, 2007) will coincide at the *lowest order* of approximation when limited to *statics*. Thus, as expected, our result for the prolate case matches that of Holsapple (2007), but is obtained within the context of a more general and flexible approach. Illustrating this will serve to provide the reader with confidence in this technique, especially when it is carried forward to consider the more complicated situation of passage into equilibrium.

We first introduce volume-averaging, and general equations governing the behavior of spinning rubble piles is obtained. This is followed by an investigation equilibrium shapes with an application to several asteroids. Finally, we probe the dynamical passage into equilibrium of spinning granular aggregates, and employ it to compare our continuum theory with n-body simulations.

2   Volume-averaging

In this section we briefly summarize the volume-averaging procedure. More details may be found in Sharma (2004), Sharma et al. (2006) or Chandrasekhar (1969).

We begin with a kinematic assumption, viz., the ellipsoid's deformation is homogeneous, i.e., ellipsoids are allowed to deform only into ellipsoids, with their centers remaining fixed. To describe this deformation, nine quantities are required to follow the time evolution of the three rotations, the three shears and the three axial stretches. This information can be encoded into a tensor (dyad) $\boldsymbol{F}$, the so-called deformation gradient, which depends only on time and that can now be used to relate the present position x of a material point to its original position X by

$$\mathsf{x} = \boldsymbol{F}\mathsf{X}. \tag{1}$$

The above is simply a mathematical representation of the kinematic constraint that ellipsoids deform into ellipsoids alone.

The above kinematic assumption is a first approximation, but was shown by Chandrasekhar (1969) to yield physically meaningful results in the case of spinning fluid masses. In fact, his results were exact in the case of inviscid fluids in pure spin. Further motivation is provided by the fact that spinning elastic ellipsoids deform into ellipsoids (Love 1946). The advantage of this assumption is that we only require the knowledge of a finite number of variables - the nine components of $\boldsymbol{F}$ - to follow the ellipsoid's deformation. We next determine a sufficient number of equations whose solution will provide the components of $\boldsymbol{F}$. The kinematic assumption (1) also serves to highlight the inherent difference between the present approach and that of Holsapple (2004). The equations employed by the latter neglect the ellipsoid's deformations, but this is sufficient for the *static* cases investigated therein. We, on the other hand, allow for the body's deformations and its effect on the subsequent dynamics by explicitly incorporating a kinematic law in Eqn. (1). Though this is only done to the lowest non-trivial order here, systematic improvements are possible by adopting a higher-order kinematic law as demonstrated by Chandrasekhar (1969) and Papadopoulos (2001). Finally, we note that that the kinematic law (1) also includes the *static* (non-deforming) case considered earlier by Holsapple (2004).

To obtain equations governing the evolution of $\boldsymbol{F}$, we begin by the standard step of taking the first moment [2] of the linear-momentum-balance equations

$$\boldsymbol{\nabla} \cdot \boldsymbol{\sigma} + \rho\mathsf{b} = \rho\ddot{\mathsf{x}},$$

where b is the body force, ρ is the body's density and $\boldsymbol{\sigma}$ is the stress, and appealing the divergence theorem to transform volume integrals, to find

$$\overline{\boldsymbol{\sigma}}V = \int_S \mathsf{t} \otimes \mathsf{x}\,dS + \int_V \rho\mathsf{b} \otimes \mathsf{x}\,dV - \int_V \rho\ddot{\mathsf{x}} \otimes \mathsf{x}\,dV, \tag{2}$$

---

[2] That is, we integrate the dyadic product ($\otimes$) of each quantity in the equation with the position vector, over the body's volume V. In indical notation, for two vectors a and b, $(\mathsf{a} \otimes \mathsf{b})_{ij} = a_i b_j$.

where $\overline{\boldsymbol{\sigma}}$ is now the average stress $(1/V) \int_V \sigma dV$ and t the traction (i.e., force per unit area) on the body's surface S.

The above equation is the same as that obtained by Holsapple (2004) and is simply a reiteration of Signorini's theorem of stress means (Truesdell and Toupin 1960, p. 574). However, this is where the present approach diverges from Holsapple's (2004). While Holsapple (2004) focuses only on the information about the average stress that he can obtain by specializing (2) to the case of a *non-deforming* body in *pure rotation* about the axis of maximum inertia, Eqn. (2) as it stands does not serve our purpose in any way because it fails to provide equations governing $\boldsymbol{F}$. We need to develop Eqn. (2) further because we are interested in investigating the *dynamics* of a *deformable* body, to the extent that is allowed by our kinematic law (1). This is done by employing (1) in (2) to represent the acceleration $\ddot{\mathsf{x}}$ in terms of the position vector x and $\boldsymbol{F}$, to yield

$$\ddot{\boldsymbol{F}} \boldsymbol{F}^{-1} \boldsymbol{I} = \int_S \mathsf{t} \otimes \mathsf{x} dS + \int_V \rho \mathsf{b} \otimes \mathsf{x} dV - \overline{\boldsymbol{\sigma}} V, \tag{3}$$

where the superscript '-1' denotes the inverse. Recognizing

$$\boldsymbol{I} = \int_V \rho \mathsf{x} \otimes \mathsf{x} dV \tag{4}$$

as the inertia dyad,

$$\boldsymbol{M} = \int_V \mathsf{x} \otimes \rho \mathsf{b} dV \tag{5}$$

as the moment tensor due to the body force b and

$$\boldsymbol{N} = \int_S \mathsf{x} \otimes \mathsf{t} dS, \tag{6}$$

as the moment tensor due to surface force ($= \mathsf{t} dS$) in (3) finally results in the volume-averaged equation

$$\ddot{\boldsymbol{F}} \boldsymbol{F}^{-1} \boldsymbol{I} = \boldsymbol{N}^T + \boldsymbol{M}^T - \overline{\boldsymbol{\sigma}} V, \tag{7}$$

where the superscript 'T' denotes the transpose. The above equation along with a constitutive equation connecting the stress $\boldsymbol{\sigma}$ to the deformation gradient $\boldsymbol{F}$ and its history $\dot{\boldsymbol{F}}$, and an evolution equation for the inertia dyad $\boldsymbol{I}$ provides a complete description to the dynamics of a homogeneously deforming ellipsoid. This is exemplified below, where we also put (7) in a form more conducive to the investigations in this paper.

Proceeding further, we note that in the case of a body in free space, the surface is traction-free ($\mathsf{t} \equiv 0$), so that $\boldsymbol{N} = 0$. Similarly the body force b is due only to internal gravity, which yields the moment tensor $\boldsymbol{M}$ from (5) as

$$\boldsymbol{M} = -2\pi \rho G \boldsymbol{I} \boldsymbol{A}, \tag{8}$$

where G is the gravitational constant and the tensor $\boldsymbol{A}$ describes the influence of the ellipsoidal shape on its internal gravity (Chandrasekhar 1969 or Sharma et al. 2006). $\boldsymbol{A}$ depends only on the axes ratios $\alpha = a_2/a_1$ and $\beta = a_3/a_1$, and is a symmetric tensor, completely known for any given ellipsoidal model of an asteroid. Relevant formulae for the components of $\boldsymbol{A}$ are given in a later section.

Introducing the velocity gradient

$$\boldsymbol{L} = \dot{\boldsymbol{F}} \boldsymbol{F}^{-1} \tag{9}$$

that relates a material point's velocity to its present position via

$$\dot{\mathsf{x}} = \boldsymbol{L}\mathsf{x}, \tag{10}$$

and using (8) for $\boldsymbol{M}$, permits (7) to be written as

$$\left(\dot{\boldsymbol{L}} + \boldsymbol{L}^2\right) \boldsymbol{I} = -2\pi\rho G \boldsymbol{A} \boldsymbol{I} - \overline{\boldsymbol{\sigma}} V, \tag{11}$$

where we have employed the symmetry of the tensors $\boldsymbol{I}$ and $\boldsymbol{A}$. Finally, post-multiplying by $\boldsymbol{I}^{-1}$ yields

$$\dot{\boldsymbol{L}} + \boldsymbol{L}^2 = -2\pi\rho G \boldsymbol{A} - \overline{\boldsymbol{\sigma}} \boldsymbol{I}^{-1} V. \tag{12}$$

The inertia dyad's evolution is governed by

$$\dot{\boldsymbol{I}} = \boldsymbol{L}\boldsymbol{I} + \boldsymbol{I}\boldsymbol{L}^T, \tag{13}$$

which is obtained by differentiating (4) while conserving mass, utilizing (10) to replace $\dot{\mathsf{x}}$ by $\boldsymbol{L}\mathsf{x}$, and finally using (4) again. Equations (9), (12) and (13) along with a suitable rheology relating the stress $\boldsymbol{\sigma}$ to $\boldsymbol{F}$ and $\boldsymbol{L}$ completely describe the *dynamics* of a homogeneously *deforming* ellipsoid in free space. By allowing a variety of material behaviors, they constitute a generalization of Chandrasekhar's (1969) virial equations to solid bodies. As demonstrated immediately below, these equations include Holsapple's (2004) calculation of the mean stress inside a *non-deforming* body as a special case.

Holsapple (2004) considered the case of an elastic-plastic ellipsoid in pure spin and in equilibrium, neglecting any deformation due to its elasticity. In this case, $\boldsymbol{L}$'s symmetric part, the *strain rate* (or *stretching*) tensor $\boldsymbol{D}$ vanishes, so that (11) simplifies to

$$\overline{\boldsymbol{\sigma}} V = \left(-2\pi\rho G \boldsymbol{A} - \boldsymbol{W}^2\right) \boldsymbol{I}, \tag{14}$$

where $\boldsymbol{W}$, the *angular velocity* (or *spin*) tensor, is the anti-symmetric part of $\boldsymbol{L}$. As we demonstrate, the above equation has the same content as the one

8

derived by Holsapple (2004), except that here (14) is derived as a particular case of the more general (11). Holsapple (2004), on the other hand, specialized (2) to the case of steady spin directly, without first introducing any kinematic assumptions to retain effects of inertia and a changing shape. Equation (14) is a balance between "centrifugal" stresses, gravitational stresses and the ellipsoid's internal strength in a volume-averaged sense. The tensor $\boldsymbol{W}$ represents the spin of the material, and is usually different from the familiar angular velocity tensor $\boldsymbol{\Omega}$ that measures the spin of an ellipsoid in terms of the rotation of its principal axes (more in Sec. 4.6). As we illustrate later, this difference is due to the presence of shear strains, and in its absence, e.g., in rigid objects, the two tensors $\boldsymbol{W}$ and $\boldsymbol{\Omega}$ are indistinguishable.

We note that when a body's allowed-deformations are restricted to homogeneous ones (i.e., ellipsoids deforming only into ellipsoids), the stresses within it are constant, so that the average stress $\overline{\boldsymbol{\sigma}}$ equals the actual stress $\boldsymbol{\sigma}$. This is because constitutive laws relate the stress to the deformation and velocity gradients $\boldsymbol{F}$ and $\boldsymbol{L}$, which are unchanged throughout the body at any fixed time. Thus, we subsequently drop the overbar on $\boldsymbol{\sigma}$. In this context, we mention that, while stresses inside objects in pure spin and tumbling objects *do* vary spatially, i.e., are *not* homogeneous. This has been shown in particular for elastic spinning ellipsoids by Chree (1889), and for elastic tumbling ellipsoids by Sharma et al. (2005).

In summary, Eqns. (9), (12) and (13) govern the motion of a homogeneously deforming gravitating ellipsoid in free space, once a constitutive law relating the stress $\boldsymbol{\sigma}$ to the body's deformation is specified. On the other hand, Eqn. (14), along with a suitable constitutive law, will help put constraints on possible equilibrium shapes. We next describe the rheology that we employ to model our asteroids.

2.1   Rheology

We can explore different material models by specifying appropriate constitutive relations, but we restrict attention to a rigid-plastic frictional material with an appropriate yield criterion. The motivation for choosing such a material description stems from the suggestion that asteroids may be granular aggregates (Richardson et al. 2002), principally held together by gravity. The crudest description of such a material's response would involve a phase where the material deforms little with the constituents remaining locked together - a phase that we will model simply as being rigid - followed by a sharp increase in deformation, as the body is stressed more, which involves the constituents slipping relative to each other and/or becoming significantly deformed. This latter behavior will be described simply by invoking a yield criterion, the vio-

lation of which instigates plastic flow. During plastic flow we will neglect the relatively small elastic deformations.

A rigid-plastic material remains rigid until failure occurs as determined by some criterion being violated, after which plastic flow begins. Because we seek to describe the behavior of granular aggregates, the yield criterion of choice must be characteristic of such materials. Thus, we could impose the condition that failure occurs when any principal stress in the material becomes tensile (positive). This *tensile criterion* captures the fact that in the absence of cohesion, granular materials cannot sustain tensile stresses. However, even when all principal stresses are compressive, the aggregate can fail if a shear stress, on some plane in its interior, overcomes the resistance due to the interaction of the aggregate's constituents. Note that even when the material comprising the aggregate is taken to be smooth, such as the smooth spheres of Richardson et al. (2005), there will be some resistance to deformation due to interlocking of the aggregate's constituents. It is possible to model this interlocking as an internal geometric friction, i.e., a frictional resistance whose origins lie in the aggregate's arrangement, rather than in the surface properties of its constituents. Thus, an appropriate yield criterion governing the transition from a rigid state, where the constituents are locked together, to a more mobile granular state that is modelled as plastic flow, could be the Mohr-Coulomb yield criterion, or its smoothed version in stress space, the Drucker-Prager criterion. Both these criteria are stated in terms of an internal friction angle, also called the angle of repose, and are discussed below. It is worthwhile pointing out that the tensile criterion is a particular case of these, when the internal friction angle is taken to be 90°. This yield criterion is shown in Fig. 2 of Holsapple (2007).

When investigating equilibrium shapes Holsapple (2001, 2004) and Sharma (2004, 2005a, 2005b) employed the Mohr-Coulomb criterion (Chen and Han 1987). This yield criterion is stated in terms of the extreme principal stresses

$$\sigma_{max} - k_{MC}\sigma_{min} \leq 0, \tag{15}$$

where k_{MC} is related to the internal friction angle ϕ_F by

$$k_{MC} = \frac{1 + \sin \phi_F}{1 - \sin \phi_F}. \tag{16}$$

Here we prefer to employ the the Drucker-Prager criterion (Chen and Han 1987) for both static and dynamical situations. This preserves continuity between the two analyses, and its smoothness facilitates numerical calculations. To formulate the Drucker-Prager yield criterion, we define the pressure p

$$p = -\frac{1}{3}\text{tr}\,\boldsymbol{\sigma}, \tag{17}$$

where 'tr' denotes the trace of the tensor, and the deviatoric stress $\boldsymbol{\sigma}'$

$$\boldsymbol{\sigma}' = \boldsymbol{\sigma} + p\mathbf{1}. \tag{18}$$

The Drucker-Prager condition can then be written as

$$|\boldsymbol{\sigma}'|^2 \leq k^2 p^2, \tag{19}$$

where $|\boldsymbol{\sigma}'|$ indicates the magnitude of the deviatoric stress as given by

$$|\boldsymbol{\sigma}'|^2 = \sigma'_{ij}\sigma'_{ij},$$

in terms of the summation convention, and

$$k = \frac{2\sqrt{6}\sin\phi_F}{3 - \sin\phi_F}, \tag{20}$$

defined so that the Drucker-Prager yield surface is the outer envelope of the Mohr-Coulomb yield surface obtained from Eqn. (15) (see Chen and Han 1988, p. 96, Fig. 2.28). As the friction angle lies between 0° and 90°, $0 \geqslant k \geqslant \sqrt{6}$. Finally, in terms of the three principal stresses σ_i, the definition above for $|\boldsymbol{\sigma}'|$ may be put into the illuminating form

$$|\boldsymbol{\sigma}'|^2 = \frac{1}{3}\left[(\sigma_2 - \sigma_3)^2 + (\sigma_3 - \sigma_1)^2 + (\sigma_1 - \sigma_2)^2\right] = \frac{2}{3}\left(\tau_1^2 + \tau_2^2 + \tau_3^2\right), \quad (21)$$

where $\tau_i = (\sigma_j - \sigma_k)/2$, $(i \neq j \neq k)$ are the principal *shear* stresses at a point, so that $|\boldsymbol{\sigma}'|$ may be thought of as a measure of the "total" local shear stress. Thus, like the Mohr-Coulomb yield criterion, the Drucker-Prager yield criterion (19), along with (20), also puts a limit on the allowable local shear stresses in terms of the local pressure and the internal friction angle. This interpretation will be found useful when we explore the yielding modes of spinning rubble piles in a later section. Finally, note that the above yield criterion assumes a cohesion-less material.

When investigating passage into equilibrium, it will be necessary to obtain stresses after the onset of plastic flow - the *plastic stresses*. In addition, we will need to formulate a law governing the material's transition from a plastic to a rigid state, akin to the yield criterion outlined above for the rigid-to-plastic transformation.

We consider first the plastic stresses. These are traditionally obtained by assuming a *plastic potential* (Chen and Han 1988), from which a *flow rule* relating the plastic stress tensor to strain rates may be derived. The plastic potential plays a role in plasticity analogous to the *work function* in elasticity (Fung 1965, Holzapfel 2001). It defines a surface in stress space that allows

the stresses to be related to strain increments[3]. For our purposes we employ
the plastic potential

$$g = \frac{1}{3}\mathrm{I}_\sigma^2 - \mathrm{II}_\sigma, \tag{22}$$

where

$$\mathrm{I}_\sigma = \mathrm{tr}\,\boldsymbol{\sigma}$$

and

$$\mathrm{II}_\sigma = \frac{1}{2}\left(\mathrm{I}_\sigma^2 - \mathrm{I}_{\sigma^2}\right)$$

are the first and second stress invariants depending only on the stress tensor's
principal values. Though it is customary to choose the yield conditions (19)
to define an *associated* plastic potential, we choose the above *non-associated*
form because it preserves volume, which is a simplifying, though not necessary,
assumption. To obtain the flow rule, we proceed by assuming that when a
body is stressed beyond yield, the incremental strain $d\boldsymbol{\varepsilon}$ (thought of as a six-
dimensional vector) is normal to the surface described by g, i.e.,

$$d\varepsilon_{ij} \sim dg/d\sigma_{ij} = \sigma'_{ij},$$

where the equality follows from differentiating formula (22). This formulation
is analogous to the one employed in the theory of elasticity to obtain con-
stitutive laws (Fung 1965, Holzapfel 2001). Introducing the proportionality
constant dq, the above can be written as

$$d\boldsymbol{\varepsilon} = \boldsymbol{\sigma}'dq,$$

which, after converting to a rate form, becomes

$$\boldsymbol{D} = \boldsymbol{\sigma}'\dot{q}, \tag{23}$$

where $\boldsymbol{D}$, as before, is the symmetric part of the strain-rate tensor that cap-
tures the stretching rates and $\dot{q}$ is again a constant. To obtain $\dot{q}$, we combine
(23) with the yield criterion (19) and obtain

$$\dot{q} = \frac{1}{kp}\left|\boldsymbol{D}\right|, \tag{24}$$

with $\left|\boldsymbol{D}\right|^2 = D_{ij}D_{ij}$ as before. Using the above in (23), we obtain the plastic
shear stress in terms of the strain rate:

$$\boldsymbol{\sigma}' = kp\frac{\boldsymbol{D}}{\left|\boldsymbol{D}\right|}, \tag{25}$$

where p is the pressure as defined in (17), and is required to maintain a
constant volume. Combining the above with (18) yields the complete plastic

---

[3] In contrast, the work function in elasticity relates stress to strain, not its incre-
ment.

stress tensor

$$\boldsymbol{\sigma} = -p\boldsymbol{1} + kp\frac{\boldsymbol{D}}{|\boldsymbol{D}|}, \qquad\qquad (26)$$

which, in component form, reads

$$\sigma_{ij} = -p\delta_{ij} + kp\frac{D_{ij}}{\sqrt{D_{kl}D_{kl}}}.$$

Note that the plastic stress depends on the strain rate through the ratio $\boldsymbol{D}/|\boldsymbol{D}|$, and so is reminiscent of dry friction with k and p playing the role of a friction coefficient and a normal force, respectively. This should be compared with the rate-dependent constitutive relations frequently employed for granular flows with low packing fractions (Jenkins and Savage 1983).

Turning now to the material's transition from a plastic rigid state, we first note that during plastic flow the material's stress state remains on the yield surface, i.e., the yield function $f = |\boldsymbol{\sigma}'|^2 - k^2p^2$ that defines the Drucker-Prager yield surface (see (19)) vanishes. This can be verified by direct substitution of the stresses from (26) into f. Consequently, during plastic flow the change $df = 0$. Simo and Hughes (1997, Sec. 2.2.2.2) and Koiter (1960, p. 173, Eq. 2.19) show that unloading takes place only when the three conditions $f = 0$, $df < 0$ *and* $\dot{q} = 0$ are together satisfied. The first of these conditions simply indicates that the material before transition is in a plastic state. The second is a requirement that post-transition to a rigid state the material must satisfy the yield condition (19) without equality. The final stipulation is equivalent to demanding that during transition the strain rate be zero. To see this, note from (24) that during plastic flow $\boldsymbol{D} \neq 0$, so that $\dot{q} > 0$. Thus, <u>for unloading from a plastic state to possibly commence, the strain rate $|\boldsymbol{D}|$ must first fall to zero</u>. In other words, plastic flow must cease before the material may transfer to a rigid state. Until this happens, $\dot{q}$ remains positive, and plastic flow continues. It is also possible for $\dot{q}$ to vanish but df to remain zero, so that the material persists in a plastic, albeit neutrally loaded state.

To summarize, we employ a rigid-perfectly-plastic material with a Drucker-Prager failure surface as a model for our asteroid. For dynamic situations, the yield criterion is coupled with an appropriate flow rule to provide stresses during plastic flow, along with suitable conditions governing transition back from a plastic to a rigid state. Throughout we assume the asteroid to be isotropic and homogenous. It should be emphasized that our ability to follow the dynamics introduced by plastic flow depends on our generalization of Chandrasekhar's (1969) virial formulation, and would not have been possible had we stopped after an application of Signorini's theorem of stress means, as Holsapple (2004, 2007) does.

2.2 Non-dimensionalization

It is possible to non-dimensionalize (12) via rescaling time by $1/\sqrt{2\pi\rho G}$, and the stress by $(3/20\pi)(2\pi\rho Gm)(4\pi/3V)^{1/3}$, where ρ, V and m are the asteroid's density, volume and mass, respectively. We obtain for (12)

$$\dot{\boldsymbol{L}} + \boldsymbol{L}^2 = -\boldsymbol{A} - (\alpha\beta)^{2/3}\boldsymbol{\sigma}\,\boldsymbol{Q}^{-1}, \tag{27}$$

where $\boldsymbol{L}$ and $\boldsymbol{\sigma}$ now represent the non-dimensional velocity gradient and average stress tensors, respectively, the derivative is with respect to non-dimensional time; α and β are the axes ratios; and $\boldsymbol{Q}$ is a non-dimensional tensor derived from the inertia tensor. In the principal-axes coordinate system of the ellipsoid, $\boldsymbol{Q}$ takes the form

$$[\boldsymbol{Q}] = \begin{pmatrix} 1 & 0 & 0 \\ 0 & \alpha^2 & 0 \\ 0 & 0 & \beta^2 \end{pmatrix},$$

where we employ square brackets to denote evaluation of a tensor in a coordinate system. The tensor $\boldsymbol{Q}$'s evolution is obtained from the non-dimensional version of (13):

$$\dot{\boldsymbol{Q}} = \frac{2}{3}\alpha\beta(\alpha\dot{\beta} + \beta\dot{\alpha})\boldsymbol{Q} + \boldsymbol{L}\boldsymbol{Q} + \boldsymbol{Q}\boldsymbol{L}^T. \tag{28}$$

Similarly, Eqn. (14), which specifies the average rigid-body stress inside a spinning asteroid in equilibrium, has the non-dimensional form

$$\boldsymbol{\sigma} = (\alpha\beta)^{-2/3}\left(-\boldsymbol{A} - \boldsymbol{W}^2\right)\boldsymbol{Q}. \tag{29}$$

The above equation has been given before by Holsapple (2004) by specializing Signorini's theorem to *non-deforming* bodies, but we obtain it as a particular case to a general *dynamic* procedure.

2.3 Coordinate system

In the following, both in static and dynamic situations, the coordinate system that we choose to evaluate the tensorial (dyadic) equations above is the one aligned with the ellipsoid's principal axes, and has an associated angular velocity tensor $\boldsymbol{\Omega}$. The advantage is that the tensors $\boldsymbol{A}$ and $\boldsymbol{Q}$ remain diagonal in this coordinate system, while the shear stresses in the 2-3 and 3-1 planes (σ_{23} and σ_{31}) are zero because of symmetry. The evaluations of the various

14

tensors in this coordinate system are

$$[\boldsymbol{A}] = \begin{pmatrix} A_1 & 0 & 0 \\ 0 & A_2 & 0 \\ 0 & 0 & A_3 \end{pmatrix} \quad [\boldsymbol{D}] = \begin{pmatrix} D_1 & D_{12} & 0 \\ D_{12} & D_2 & 0 \\ 0 & 0 & D_3 \end{pmatrix}$$

$$[\boldsymbol{\sigma}] = \begin{pmatrix} \sigma_1 & \sigma_{12} & 0 \\ \sigma_{12} & \sigma_2 & 0 \\ 0 & 0 & \sigma_3 \end{pmatrix} \quad [\boldsymbol{W}] = \begin{pmatrix} 0 & -W_3 & 0 \\ W_3 & 0 & 0 \\ 0 & 0 & 0 \end{pmatrix},$$

with $\boldsymbol{\Omega}$ having the same form as $\boldsymbol{W}$, and $\boldsymbol{Q}$'s structure was indicated in the previous section. Recall that the A_i ($i = 1, 2, 3$) depend only on the axes ratios α and β.

2.4 The components A_i

The A_i obey the useful relation $A_1 + A_2 + A_3 = 2$ (Chandrasekhar 1969), so that for a given ellipsoid we only need to specify two of the three A_i. For oblate spheroids ($1 = \alpha > \beta$) we have

$$A_1 = A_2 = -\frac{\beta^2}{1 - \beta^2} + \frac{\beta}{(1 - \beta^2)^{3/2}} \sin^{-1}\sqrt{1 - \beta^2}, \tag{30}$$

while for prolate[4] objects ($1 > \alpha = \beta$),

$$A_2 = A_3 = \frac{1}{1 - \beta^2} - \frac{\beta^2}{2(1 - \beta^2)^{3/2}} \ln \frac{1 + \sqrt{1 - \beta^2}}{1 - \sqrt{1 - \beta^2}}, \tag{31}$$

and finally for truly triaxial ellipsoids ($1 > \alpha > \beta$)

$$A_1 = \frac{2\alpha\beta}{(1 - \alpha^2)\sqrt{1 - \beta^2}} (F(r, s) - E(r, s)) \tag{32}$$

and

$$A_3 = \frac{2\alpha\beta}{(\alpha^2 - \beta^2)\sqrt{1 - \beta^2}} \left(\frac{\alpha}{\beta}\sqrt{1 - \beta^2} - E(r, s) \right), \tag{33}$$

where F and E are elliptic integrals of the first and second kinds (Abramowitz and Stegun 1965), respectively, with the argument $r = \sqrt{1 - \beta^2}$ and parameter $s = \sqrt{(1 - \alpha^2)/(1 - \beta^2)}$.

---

[4] Note that the formula for A_3 given in Sharma et al. (2006) is incorrect, as it has a spurious square root over the first term.

3   Example: Statics

Consider now an application of the above volume-averaging approach to the equilibrium shapes of ellipsoids spinning about the 3-axis with $1 \geqslant \alpha \geqslant \beta$. We will consider a spinning ellipsoidal asteroid, initially taken to be rigid. The average internal stresses within such a body are given by (29) as a function of its spin and its axes ratios α and β. Knowing the stresses will then allow us to employ an appropriate yield criterion to map out regions parameterized by the asteroid's spin and its shape within which it can exist in equilibrium. Note that because asteroids at equilibrium are rigid, the spin tensor $\boldsymbol{W}$ and the angular velocity tensor $\boldsymbol{\Omega}$ are the same, so that W_3 is, in fact, the same as the rate Ω_3 at which the asteroid rotates about its 3-axis; cf., (52) and the discussion thereafter.

When discussing rheology in Sec. 2.1, we outlined two possible yield criteria. Equilibrium configurations based on an application of the Mohr-Coulomb yield criterion were first reported by Holsapple (2001, 2004) and also independently derived by Sharma (2004). Here we present complete results based on the Drucker-Prager yield criterion. This law was first applied to spinning rubble piles initially in a dynamical context by Sharma (2004) and then also for statics by Sharma et al. (2005). Recently, Holsapple (2007), working with the formulation of Holsapple (2004), too utilized this yield criterion in his static calculations, and provided only a figure detailing the equilibrium shapes for spinning prolate ellipsoids. Here we supplement his published results by giving the equations describing the equilibrium landscape, and also applying them to previously unconsidered oblate and triaxial shapes.

From his figure for prolate ellipsoids, Holsapple (2007) notes that the effect of employing the smoother Drucker-Prager yield criterion is to iron out kinks in the results obtained from the Mohr-Coulomb yield criterion. But, as we will see, there are other effects also, the most notable of which is the widening of the allowable equilibrium zone for any fixed friction angle ϕ_F. This is especially pronounced for friction angles greater than 20°; friction angles particularly appropriate for rubble piles. Further, the lower bound observed for all ϕ_F at any fixed axes ratio α with the Mohr-Coulomb law, now vanishes at a particular friction angle that depends on α. This will affect our interpretations of computational results. In particular, we will see in Sec. 4.5 that employing a Drucker-Prager yield criterion leads to a more satisfying comparison with the results of Richardson et al. (2005). Further, this expansion of the equilibrium zone may have important implications on predictions about an object's interior; objects thought to be monolithic based on a Mohr-Coulomb analysis may now be considered to be rubble piles.

In addition to providing new results, there are other benefits to presenting the

static analysis of this section. As we have stressed all along, our dynamical formulation in the special case of *statics* collapses to Holsapple's (2004) development, which was based on a restricted application of a theorem due to Signorini. Thus, comparison of the static results of this section with ones obtained earlier by Holsapple (2007) will engender confidence in our technique. Furthermore, it also provides completeness to our work, in the sense that it presents a unified way to look at *static* configurations of spinning rubble-pile ellipsoids, and the *dynamical* processes by which such spinning configurations are obtained in particle simulations (Richardson et al. 2005), thereby allowing a better comparison between continuum results and the discrete model of Richardson et al. (2005). Finally, an application of the present approach to the simple case of statics will help prepare the reader for the more complicated situation of dynamics.

This section thus provides new equilibrium results obtained by an application of a yield criterion that easily extends to a dynamical situation. We begin by first reporting the equations that generate the equilibrium landscape for a spinning rubble pile modeled as a rigid-perfectly-plastic triaxial ellipsoid obeying a Drucker-Prager yield criterion.

3.1   *The equilibrium landscape for a general triaxial ellipsoid*

Burns and Safronov (1973) and Sharma et al. (2005a) predict that internal energy dissipation will drive a solid body to a state of pure spin about its axis of maximum inertia. Thus, we consider only the case when $1 > \alpha > \beta$. Eqn. (29) provides the average stresses inside the rigid asteroid as

$$\sigma_1 = \left(W_3^2 - A_1\right)(\alpha\beta)^{-2/3}, \tag{34}$$

$$\sigma_2 = \alpha^2 \left(W_3^2 - A_2\right)(\alpha\beta)^{-2/3} \tag{35}$$

and

$$\sigma_3 = -\beta^2 A_3 \left(\alpha\beta\right)^{-2/3}. \tag{36}$$

At the outset we recognize that because rubble piles cannot support tensile stresses, each of the above principal stresses must be negative, i.e., compressive. However, this is just a necessary requirement. In order for the asteroid to not fail, the above average stresses must not violate the Drucker-Prager yield criterion given by (19). To this end, we first employ the above formulae for the stress $\boldsymbol{\sigma}$ in (17) to calculate the pressure p and then use (18) to calculate the deviatoric stress $\boldsymbol{\sigma}'$. Substituting $\boldsymbol{\sigma}'$ and p into the yield criterion (19) generates an inequality that is quadratic in W_3^2. The inequality itself is parameterized by k that in turn depends on the friction angle ϕ_F through (20). The solution of this inequality for a fixed ϕ_F (hence k) yields, in general, two positive and two negative solutions for W_3 in terms of the axes ratios α and β.

Recall that the functions A_i described in Sec. 2.4 depend on these axes ratios alone. The negative spins can be disregarded as they simply identify an opposite spin state. The positive roots bound a region in the three dimensional spin (W_3) and shape (α, β) space within which a spinning triaxial rubble pile can exist in equilibrium.

The two critical solutions to the inequality obtained after an application of the Drucker-Prager criterion (19) are given by the positive square roots of

$$W_3^2 = \frac{1}{q_1 + q_2} \left(q_1 A_1 + q_2 A_2 + q_3 A_3 \pm 3\sqrt{D} \right) \tag{37}$$

where

$$
\begin{aligned}
q_1 &= (1 + \alpha^2)(3 + k^2) - 9, \\
q_2 &= \alpha^2(1 + \alpha^2)(3 + k^2) - 9\alpha^4, \\
q_3 &= \beta^2(1 + \alpha^2)(3 + k^2),
\end{aligned}
\tag{38}
$$

and $D = d_{ij} A_i A_j$, in terms of

$$d_{11} = d_{22} = -d_{12} = -d_{21} = -2\alpha^4 \left(\frac{3}{2} - k^2 \right),$$

$$d_{33} = \beta^4 \left(9\alpha^2 - 2(1 + \alpha^2 + \alpha^4) \left(\frac{3}{2} - k^2 \right) \right),$$

and

$$d_{23} = d_{32} = -d_{31} = -d_{13} = \alpha^2 \beta^2 (1 - \alpha^2)(3 + k^2).$$

The solutions for W_3 given by (37) delineate surfaces for a fixed k that correspond to a particular friction angle ϕ_F via (20). Thus, we would in general expect both a lower and an upper bounding surface at any ϕ_F. We explore several values of the friction angle in Figs. 1 and 2. In these figures, because we stipulate that $1 \geqslant \alpha \geqslant \beta$, the surfaces are abruptly truncated by the plane $\alpha = \beta$. As shown in Figs. 1(a), 1(b), 2(a) and 2(b), there are indeed two such surfaces at lower friction angles that separate from each other with increasing internal friction. The solution with the positive square root of D in (37) defines the lower bound, while the other solution establishes the upper surface. Any triaxial ellipsoid with an internal friction angle ϕ_F whose axes ratios α and β, and spin W_3 are such that it lies between the two bounding surfaces corresponding to that ϕ_F, can exist in equilibrium. We see from Figs. 1(a) and 1(b) that as the friction angle drops to zero the two surfaces come closer together, ultimately pinching off at $k = 0$ ($\phi_F = 0$) to reveal the famous Maclaurin and Jacobi curves (highlighted in these figures) on which spinning fluid ellipsoids may exist in equilibrium (see Chandrasekhar 1969). The equations for these curves may be obtained by setting $k = 0$ in (37). For example, the Jacobi
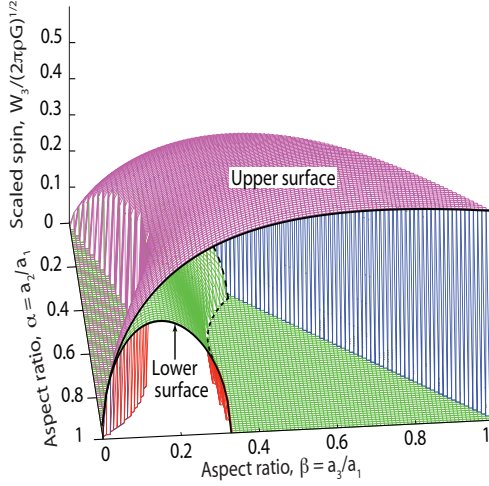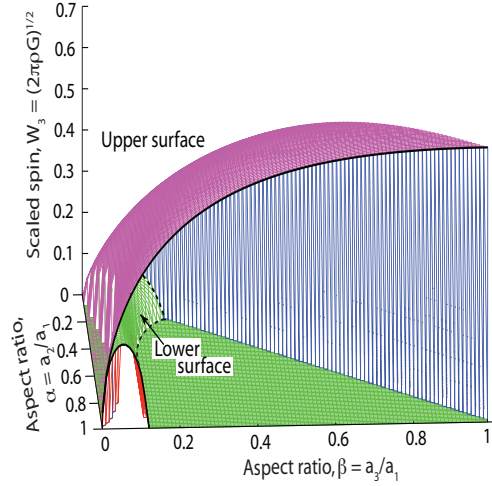
18
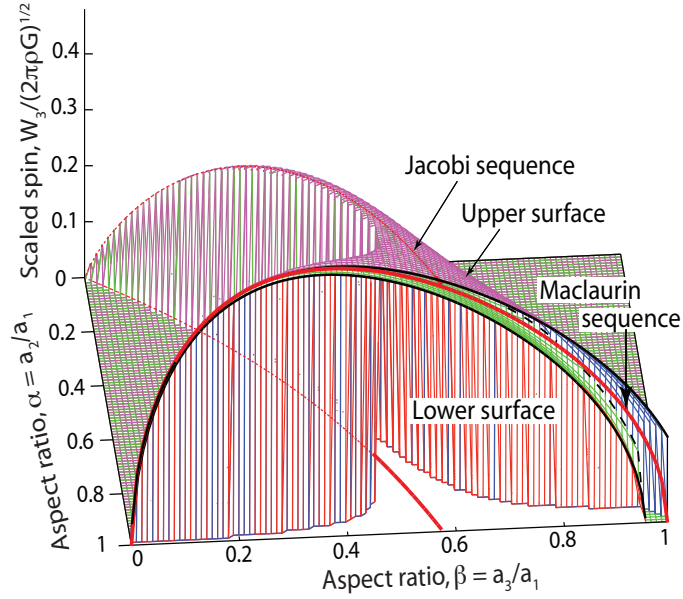
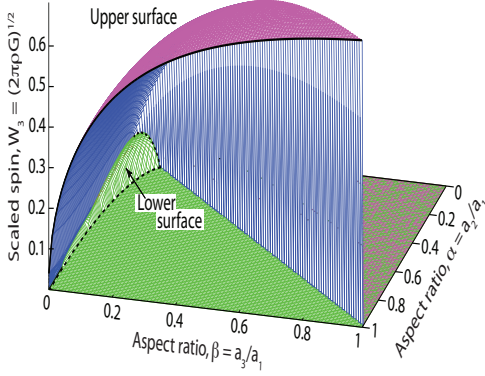(a) Friction angle, $\phi_F = 1^o$.
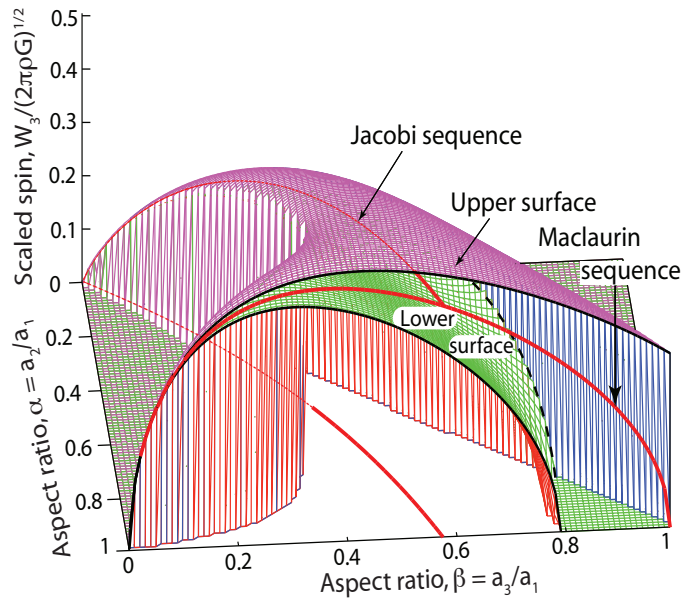
(b) Friction angle, $\phi_F = 5^o$.

Fig. 1. The three-dimensional equilibrium landscape in shape-spin (α, β, W_3) space for two very low friction angles ϕ_F. The equilibrium region is the volume enclosed by the upper and lower surfaces. These two bounding surfaces have the shape of slender caverns that widen sharply near $\alpha = 1$. These surfaces come infinitesimally close as ϕ_F approaches zero, ultimately pinching off to reveal the Jacobi and Maclaurin sequences. These sequences are indicated by the space curve that lies in between the two surfaces. Also shown is the projection of the Jacobi curve on the $W_3 = 0$ plane. The dashed curve is the intersection of the upper and lower surfaces.

19

(a) Friction angle, $\phi_F = 20^o$.

(b) Friction angle, $\phi_F = 30^o$.

(c) Friction angle, $\phi_F = 36.9^o$.
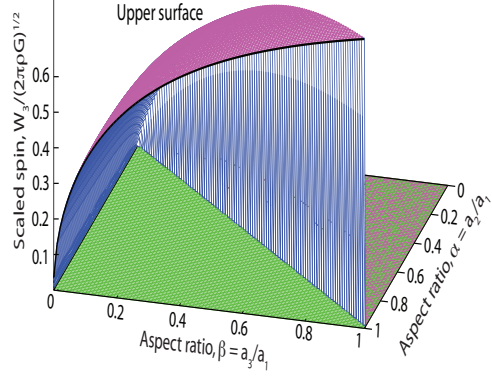
(d) Friction angle, $\phi_F = 90^o$.

Fig. 2. Continuation of Fig. 1. The three-dimensional equilibrium landscape in shape-spin (α, β, W_3) space for intermediate to large low friction angles ϕ_F. As ϕ_F increases, so does the equilibrium region. The upper surface lifts, while the lower surface shrinks, before beginning to disappear for $\phi_F \geqslant 36.9^o$. By $\phi_F = 90^o$, the lower bound vanishes completely. The dashed curves are the intersections of the lower surface with the upper surface and with the plane $W_3 = 0$.

curve relevant for fluid ellipsoids with $1 > \alpha > \beta$ is simply,

$$W_3^{Jacobi} = \left[\frac{A_1(\alpha, \beta_J) - \alpha^2 A_2(\alpha, \beta_J)}{1 - \alpha^2} \right]^{1/2},$$

where β_J satisfies the non-linear equation

$$\beta = \frac{\alpha\sqrt{(1 - \alpha^2)A_3(A_2 - A_1)}}{(1 - \alpha^2)A_3}$$

20

obtained from the requirement that in (37), $D \geqslant 0$. Recall that the functions A_i depend on α and β, and were defined in Sec. 2.4.

From Fig. 2(c) we note that the lower bounding surface ceases to exist at higher friction angles for α's greater than some value. This is in contrast to what was observed for a Mohr-Coulomb yield criterion by Holsapple (2001) and Sharma (2004), where this surface survived for all α until ϕ_F equalled 90°. In fact, the lower bound here begins to vanish for $k \geqslant \sqrt{3/2}$, which corresponds to a friction angle $\phi_F \geqslant \sin^{-1}(3/5) \approx 36.87^o$. For these k, the denominator $q_1 + q_2$ in (37) that depends only on α, admits a positive root $\alpha(k) = \left(k^2 + 3 - 3\sqrt{2}\sqrt{k^2 - 3/2} \right) / (6 - k^2)$. At this $\alpha(k)$, the solution corresponding to the lower surface in (37) becomes unbounded, thereby making the lower bound inapplicable for $\alpha > \alpha(k)$. As the internal friction further increases, the bottom surface becomes progressively insignificant, ultimately disappearing altogether at $\phi_F = 90^o$ as in the Mohr-Coulomb case (see Fig. 2(d)). However, the solution describing the upper surface approaches a definite limit at $k = \sqrt{3/2}$, and so survives. Again, a body that lies below the surviving upper bounding surface corresponding to the body's internal friction angle remains intact.

Finally, any object whose spin and shape parameters place it outside the $\phi_F = 90^o$ upper bounding surface in Fig. 2(d) cannot survive as a rubble pile. This is because a friction angle of 90° corresponds to sticking friction, so that the body can only fail if one of the principal stresses becomes tensile. However, a *cohesionless* rubble pile cannot sustain any tensile stress.

To better understand the two bounding surfaces obtained above, we investigate the effect of varying the spin rate on an ellipsoid's equilibrium. Suppose the spin W_3 and the axes ratios α and β for an ellipsoid are so chosen that they permit an equilibrium solution. If now we keep these axes ratios constant and increase W_3, "centrifugal" effects along the 1- and 2- axes decrease the compressive stresses $|\sigma_1|$ and $|\sigma_2|$, i.e., σ_1 and σ_2 becomes less negative. We recall that the internal average principal stresses of (34) - (36) must always be negative. Because the 3-axis is the spin axis, the stress σ_3 along it remains unchanged. Thus, raising the spin augments the magnitudes of the shear stresses $\tau_2 = (\sigma_3 - \sigma_1)/2$, and $\tau_1 = (\sigma_2 - \sigma_3)/2$. At the same time, for cases when $\alpha \neq 1$, (34) and (35) indicate that the third principal stress $\tau_3 = (\sigma_1 - \sigma_2)/2$ may also increase in absolute value. As the spin continues to increase, so do the $|\tau_i|$, which in turn amplifies the magnitude of the deviatoric stress tensor $|\boldsymbol{\sigma}'|$ that enters the right hand side of the Drucker-Prager yield criterion (19), leading ultimately to failure. Recall from (21) that $|\boldsymbol{\sigma}'|$ is influenced directly by the size of the principal shear stresses τ_i. This failure, which corresponds to the ellipsoid being pushed beyond the upper bounding surface in spin-shape space, is driven by an increase in "centrifugal" stresses, and so can be thought

of as "rotation-driven failure". It should be pointed out that although this terminology may suggest that the body is torn apart, the failure is really due to increased shear stresses within the body.

Now suppose the spin of the body is reduced, once more keeping the ratios α and β fixed. In this case, the compressive stresses along the 1- and 2- axes increase due to a decrease in "centrifugal" stresses. As before, σ_3 remains unchanged. There is again a possibility that differences between the σ_i may magnify the principal shear stresses enough to cause the body to yield as it goes through the lower bounding surface. Because at low enough speeds the principal stresses in this case are all dominated by gravity, we term this failure mode as "gravity-driven failure". Again note that this term does not indicate an implosion of the body, but rather shear failure due to gravitational effects. Of course, this mode of failure is only viable when the lower bound exists for the chosen α and β.

To gain more insight, we now specialize the results of this section to three important cases. These cases correspond to viewing particular sections of the three dimensional surfaces described above.

3.2 Oblate ellipsoids: $\alpha = 1 \geqslant \beta$

Oblate ellipsoids have $a_2 = a_1$, so that $\alpha = 1$ and $A_1 = A_2$. The solutions (37) now simplify to

$$W_3^2 = A_1 + \frac{k \pm \sqrt{6}}{2k \mp \sqrt{6}} \beta^2 A_3. \tag{39}$$

The critical speeds obtained above correspond to curves that separate the shape (β) - spin (W_3) parameter space into different regions. These region-defining curves themselves are parameterized by k that in turn depends on the internal friction angle ϕ_F. Several of them are plotted in Fig. 3. The contours are the intersections of the three dimensional surfaces shown in Figs. 1 and 2 with the plane $\alpha = 1$. The equilibrium landscape thus obtained is similar to the one previously obtained by employing the Mohr-Coulomb yield criterion (see Fig. 2 of Holsapple 2001, or Fig. 7 of Holsapple 2004). For comparison, the Mohr-Coulomb solutions of Holsapple (2001) are included as dashed curves in Fig. 3. The curve obtained with $\phi_F = 0^o$ (so that $k = 0$) concerns invisicid fluids, and represents Maclaurin spheroids as discussed by Chandrasekhar (1969).

From Fig. 3, we see that for low friction angles ϕ_F, there are upper and lower bounds to the angular velocity W_3 that can be supported at a given shape β. The upper curve is obtained by choosing the negative sign in the numerator and positive in the denominator. Interestingly, the upper limiting curve is
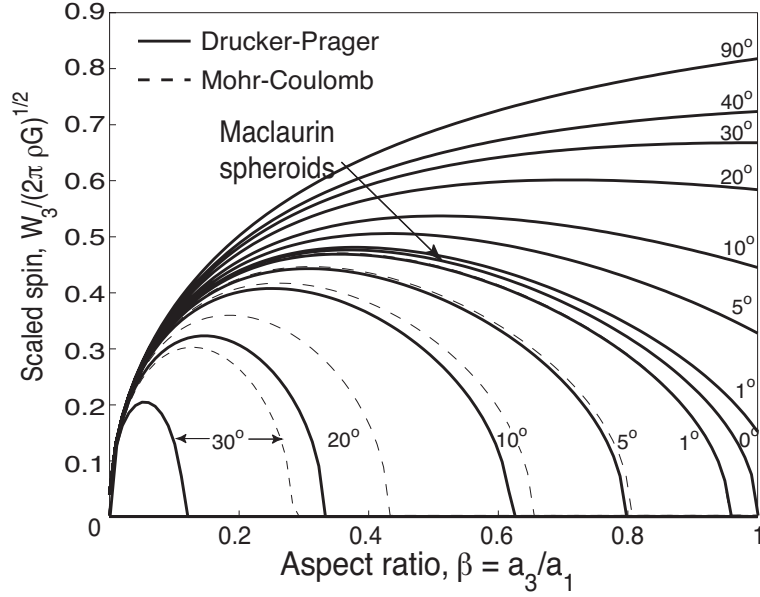
Fig. 3. Regions in spin-shape space where an oblate ellipsoidal asteroid that obeys a Drucker-Prager yield criterion can exist in equilibrium. Numbers next to the curves indicate the corresponding friction angle ϕ_F. For a particular ϕ_F, different shapes occur for spins faster or slower than that of a Maclaurin spheroid. The dashed curves are for a Mohr-Coulomb material (from Holsapple 2001). Because the object spins as a rigid body, the spin W_3 equals Ω_3 ,the rotation rate of the ellipsoid's principal axes.

exactly the same as the one obtained by employing a Mohr-Coulomb yield criterion. This can easily be seen by substituting for k from (20) in (39) and comparing with Eq. (8.7) of Holsapple (2004). In contrast, Fig. 3 reveals that the Drucker-Prager lower bound is much less stringent than the corresponding one due to the Mohr-Coulomb law. In fact, the former lower bound disappears for $\phi_F = \sin^{-1}(3/5)$ that corresponds to $k = \sqrt{3/2}$. This is the value of k at which the denominator of the corresponding root in (39) vanishes. Note that only the root yielding the lower curve is ill-behaved, as was indicated in the previous section's discussion. In Sec. 3.6 we employ the bounds obtained here to asteroids previously not considered.

3.3   Prolate ellipsoids: $1 \geqslant \alpha = \beta$

For prolate ellipsoids, (37) reduces to

$$W_3^2 = \frac{1}{q_1 + q_2}\left[(1+\alpha^2)(3+k^2)(A_1 + 2\alpha^2 A_3) - 9(A_1 + \alpha^4 A_3) \pm 3\sqrt{D}\right] \quad (40)$$
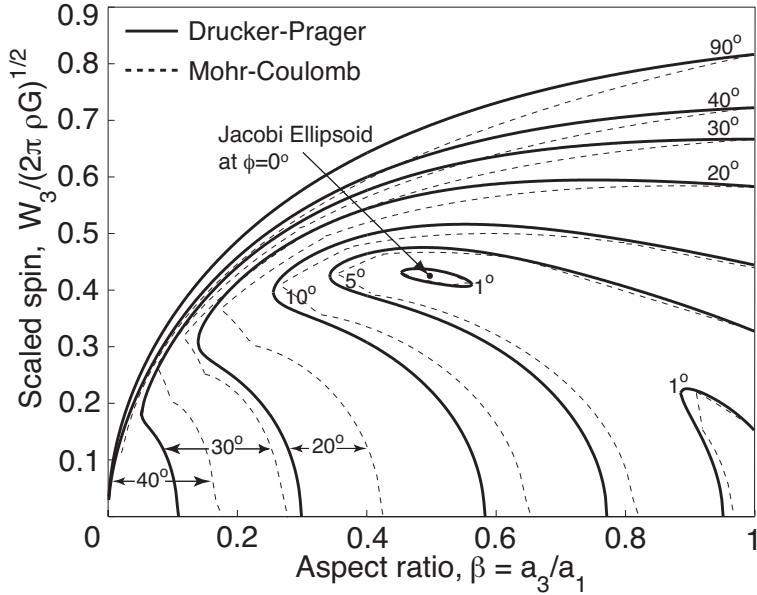
23

Fig. 4. Regions in spin-shape space where a triaxial ellipsoidal asteroid that obeys a Drucker-Prager yield criterion can exist in equilibrium. We have chosen the special circumstance where the axes ratios α and β are related by $2\alpha = 1+\beta$. Numbers next to the curves indicate the corresponding friction angle ϕ_F. The dashed curves are for a Mohr-Coulomb material as obtained by Holsapple (2001). Because the object spins as a rigid body, the spin W_3 equals Ω_3, the rotation rate of the ellipsoid's principal axes.

where q_1 and q_2 were given by (38), and D simplifies to

$$
D = 2\left(k^2 - \frac{3}{2}\right)A_1^2 + (-6k^2 + 6\beta^2 + 2k^2\beta^2)A_3 A_1 + (6k^2 + 2k^2\beta^4 - 3\beta^4)A_3^2
$$

The resulting curves, which are the intersections of the surfaces in Figs. 1 and 2 with the plane $\alpha = \beta$, were first plotted for $\phi_F = 40^o$ by Sharma et al. (2005). Later, Holsapple (2007) provided curves for several other friction angles. Because the equations above generate exactly Fig. 7 of Holsapple (2007), we omit graphing these curves. However, later, Fig. 6 plots several known asteroids relative to the equilibrium bounds obtained here.

Analogous to the oblate case, the critical curves obtained from (40) divide the W_3 - β space into zones parameterized by the internal friction angle ϕ_F. At low friction angle ϕ_F, there is an upper and a lower bound to the angular velocity W_3 that can be supported at a given β. The upper and lower bounds are obtained by choosing the negative and positive signs in (40), respectively. In contrast to oblate ellipsoids, the only solution possible for the case of $\phi_F = 0^o$, i.e., an inviscid fluid, is a stationary sphere ($\alpha = \beta = 1$ and $W_3 = 0$).

24

3.4 Triaxial ellipsoids: $\alpha = (1 + \beta)/2$

As a final example to aid in visualizing the three dimensional topography of Figs. 1 and 2, we follow Holsapple (2001) and intersect those surfaces with the plane defined by $2\alpha = 1 + \beta$. This produces Fig. 4, which is thus the equilibrium landscape associated with triaxial ellipsoids whose intermediate axis is the mean of the other two. The equations defining these curves may be recovered from (37) by substituting $(1 + \beta)/2$ for α. It is possible to construct similar figures for triaxial ellipsoids whose axes ratios relate differently.

Again, the curves are smoother incarnations of ones obtained by Holsapple (2001) with a Mohr-Coulomb yield criterion. These latter ones are displayed in Fig. 4 by dashed lines. We immediately note that, for friction angles beyond 20°, the Drucker-Prager yield criterion provides a much larger equilibrium region than the Mohr-Coulomb yield criterion. The intersection of the Jacobi curve (see Sec. 3.1) with the plane $2\alpha = 1 + \beta$ locates the point in Fig. 4 that is thus the only allowed fluid ellipsoidal shape whose intermediate axis is an average of the other two. The upper and lower bounds to the angular velocity W_3 that can be supported at a given β at any given friction angle ϕ_F, have previously been identified with rotation-driven, or gravity-driven failure. Fig. 7 below will show that many known asteroids fall well within the zones of equilibrium readily identified with granular aggregates.

3.5 Discussion

By using stresses from (29) in conjunction with the Drucker-Prager yield criterion (19) at equality, we obtained critical surfaces for the spin W_3 in terms of the axis ratios α and β. We saw that, for low friction angles, an upper and a lower surface bound a region within which a stable spinning ellipsoid is possible. It was also indicated that the region of possible equilibrium shapes encompassed by the critical surfaces was larger than that obtained for Mohr-Coulomb materials, especially for friction angles beyond 20°. We further observed that the lower bound existed only for restricted values of the axes ratio α for internal friction angles greater than 36.87^o. This is in contrast to solutions obtained by an application of the Mohr-Coulomb yield criterion (Holsapple 2001). Failure was understood by identifying the sources of shear stresses at failure. Known solutions for inviscid fluids were recovered by setting the internal friction angle to zero. Finally, we also probed these surfaces by intersecting them with planes corresponding to some special, but important, ellipsoidal geometries.

The constraints on spin and shape for rigid-perfectly-plastic materials with a

Drucker-Prager yield criterion match Holsapple (2007) in the one case (prolate ellipsoids) that he reports. In addition, our volume-averaged solutions have the same general characteristic as Holsapple's (2001) exact results. Differences are due only to our employing a distinct yield criterion. If we too had employed the Mohr-Coulomb yield criterion that Holsapple (2001) does, the comparison would have been perfect. This was noted previously by Holsapple (2004, 2007) and Sharma (2004). Conversely, if exact results were to be obtained using Holsapple's (2001) limit analysis procedure along with a Drucker-Prager yield criterion, there will be strict correspondence with our results. To see this, we first invoke (21) and (17) to phrase the yield condition (19) entirely in terms of ratios of the principal stresses σ_i. In this homogenized form, the spatially varying nature of the stresses employed by Holsapple (2001) is suppressed, and we recover (37) exactly.

This exact match between predictions of a volume-averaged procedure and one based on limit analysis is surprising. There is, to our knowledge, no formal explanation available as to why and when these two approaches converge. Here we attempt a heuristic justification. In the first method, volume-averaged stresses are used to test for incipient yield on the average. Because yielding is usually initiated locally, this suggests that the present approach should be analogous to a *local* analysis. In contrast, limit analysis, i.e., a categorization of loading situations beyond which the body cannot possibly survive, seeks *global* failure, while using spatially varying stress fields. Thus, it might be expected that results of volume-averaging be more sensitive than those of limit analysis, as these latter results are the envelope of all other yield solutions. However, here we impose yield conditions on the *average* stress field, thereby requiring the body to yield on average. This is a stronger stipulation, as a body that yields on average must necessarily have yielded locally to a sufficient extent. Indeed, as Holsapple (2004) points out, the reason his volume-averaged results reproduce findings of Holsapple's (2001) limit analysis, is because in the latter analysis the limit-failure solution predicts that the entire ellipsoid yields simultaneously, so that yielding at a point coincides with global failure. It appears that enforcing yielding on the average effectively globalizes the yield conditions, making them comparable to those required for global failure.

It is worthwhile to note that the volume-averaged approach may not yield the same answers as limit analysis in all situations. This has been confirmed recently by Holsapple (2007) in his investigation of the equilibrium shapes of spinning ellipsoids with cohesion.

Finally, in order to profitably utilize the equilibrium landscapes derived above for ellipsoids, it is necessary to note the effect of surface irregularities because no asteroid is perfectly ellipsoidal. As Holsapple (2001) mentions, asteroids with shapes deviating from their best-fit ellipsoids will have perturbations in the stress field obtained by assuming an ellipsoidal shape. If the unevenness is

on a scale larger than the constituting particle size of the granular aggregate, then the perturbation in the stress field will locally violate the yield criterion. Thus, for an asteroid modeled as a Drucker-Prager material to survive, it is necessary for its nominal ellipsoid[5] to exist. In other words, for an asteroid to exist as a rubble pile with some internal friction angle ϕ_F, a necessary condition is for its associated ellipsoidal shape to lie within the equilibrium curves associated with that ϕ_F (and that ellipsoidal shape).

3.6   Applications

Figures 5, 6 and 7 plot the equilibrium landscape in spin-shape space. To these diagrams we have added the positions of several asteroids. The rotation and the best-fit ellipsoidal shape of these asteroids were obtained by Kaasalainen et al. (2002), Torppa et al. (2003) and Kaasalainen et al. (2004) from photometric data. The physical properties of all near-Earth objects (including 1036 Ganymed, 1580 Betulia, 2100 Ra-Shalom, 3103 Eger, 3199 Nefertiti, 4957 Brucemurray, 5587 1990 SB and 6053 1990 BW3, which are given in Figs. 5 - 7) can be found at http://earn.dir.de. We assume the average density ρ of these bodies to be 2 g cm^{-3}. We comment on the effects of different densities below. It is important to point out that in the case of asteroids with approximately triaxial shapes, we restricted ourselves to a selection whose axes ratios were related by $2\alpha = 1 + \beta$. In order to consider asteroids whose nominal triaxial ellipsoids had differently related axes ratios we would simply have to redraw Fig. 7 with that appropriate relation.

From Figs. 5, 6 and 7, we see that almost all the asteroids tend to lie between the equilibrium curves corresponding to a friction angle ϕ_F of 10°. This indicates a relatively weak tensile strength is sufficient to preserve coherence in these asteroids, and reinforces the widely held view that these objects are rubble piles. An exception is provided by asteroid 6053 (1993 BW3), classified as an S object, in Fig. 5 that lies beyond the region demarcated by a friction angle ϕ_F of even 90°. Recall that a ϕ_F of 90° characterizes a material that is resistant to any amount of shear, and so can fail only under a tensile load. Thus, we can with some confidence now propose that asteroid 6053 (1993 BW3) has some tensile strength and is most probably a monolithic body, not too surprising for a 3-km. near-Earth asteroid. However, if this body's density were larger than, e.g., 3 g cm^{-3}, then its scaled spin drops closer to 0.5, in which case its status as a monolith is in considerable doubt. Unfortunately, 6053's classification is uncertain; various authors have placed it as a S, QR or an Sq (see the EARN database).

4957 Brucemurray in Fig. 7 is a near-Earth asteroid (NEA) classified as an S

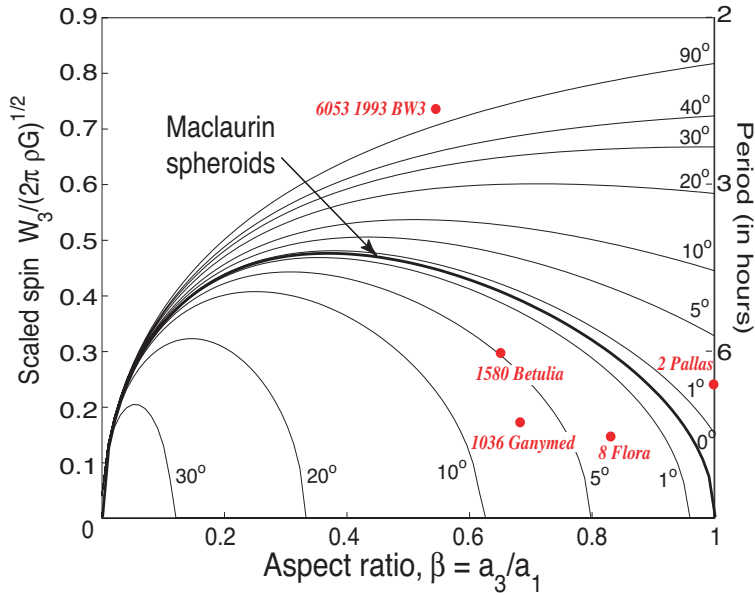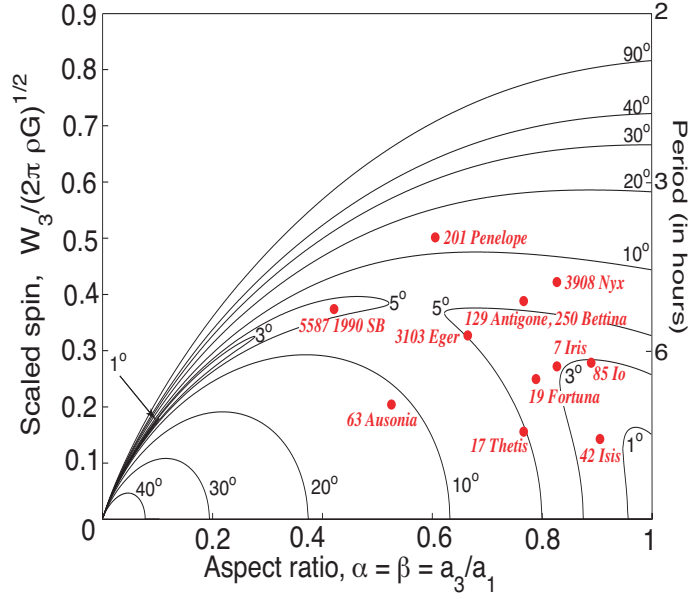[5]   Obtained by smoothening irregularities over several particle lengths

Fig. 5. Positions of several approximately oblate asteroids in spin-shape space. Numbers next to the curves indicate the corresponding friction angle ϕ_F.

object that has a scaled spin 0.64, and best-fit ellipsoidal axes ratios $\alpha \approx 0.91$ and $\beta \approx 0.83$, so that $2\alpha \approx 1 + \beta$. These parameters place it near the upper edge of the equilibrium region that contains all possible triaxial ellipsoids with $2\alpha = 1 + \beta$ and $\phi_F \leqslant 30^o$. Because the ϕ_F's of most natural aggregates range between 20° and 40°, this location suggests that unless 4957 Brucemurray has some tensile strength (possibly due to cohesion), it is poised on the verge of failure, and just a small increase in its spin could disrupt it.

Figures 5 - 7 also allow us to explore how errors in an asteroid's assumed density may affect our perception of its rubble-pile nature. The nominal densities corresponding to a particular class of asteroid are not well constrained, nor are the classifications of these objects, especially for NEAs, because of the rapidly varying phase of close objects. If the actual density of an asteroid were less than what we assume, then it would have the effect of increasing its scaled spin, thereby pushing it into a regime that necessitates more internal friction for survival. For example, if 3199 Nefertiti (a 2-km. NEA that may be either an S or an A object) in Fig. 7 had a density 1.4 g cm^{-3} rather than 2 g cm^{-3} as presumed, then its scaled spin would increase from the present value of 0.61 to 0.71. At this higher scaled spin, 3199 Nefertiti would require an internal friction angle of nearly 40° to support itself. This would again indicate that either 3199 Nefertiti has some tensile strength, or that it is precariously poised on the edge of failure. Similarly, if in Fig. 6, 3908 Nyx had a density 1 g cm^{-3}, its scaled spin would increase to about 0.59, from its nominal value of 0.42. This would suggest that for Nyx to survive as a prolate ellipsoids, it should have an internal friction angle of about 20°, a value perhaps not commensurate with the low density of 1 g cm^{-3}, as we expect less densely packed objects

Fig. 6. Positions of several <u>approximately prolate</u> asteroids in spin-shape space. Numbers next to the curves indicate the corresponding friction angle ϕ_F. The equilibrium landscape follows that of Holsapple (2007, Fig. 7)
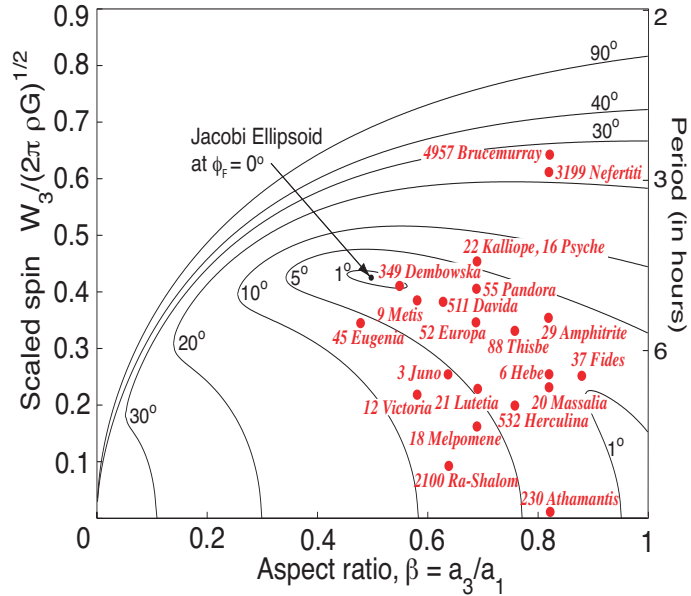

Fig. 7. Positions of several <u>triaxial</u> asteroids in spin-shape space. In the triaxial case, we have chosen the special circumstance where the axes ratios α and β are related by $2\alpha = 1 + \beta$. Numbers next to the curves indicate the corresponding friction angle ϕ_F.

to be less resistant to shear, i.e., to have lower internal friction. This latter expectation stems from the observation that a significant contribution to a rubble pile's internal friction is from its packing, i.e., the granular medium's resistance to shear due the finite size of its constituent objects; Richardson

29

et al. (2005) call this the *cannonball-stacking* effect. Thus, this *geometric* friction is independent of surface roughness[6], but depends directly on the pile's packing density.

By contrast, the large asteroids 129 Antigone, 201 Penelope and 250 Bettina, all of which appear in Fig. 6, are believed to be M asteroids. If this designation is correct and if M asteroids have the expected heavy densities, their scaled spins would shift much lower.

With the exception of shapes determined by radar or spacecraft (cf. Ostro et al. 2002), our axial ratios are derived by the inversion of lightcurve data (e.g., Kaasalainen et al. 2004). We have accepted the shapes coming from such an approach for lack of better options, but we recognize that they may contain some errors.

4   Example: Dynamics

We now demonstrate how our method can be extended beyond purely *static* approaches such as those of Holsapple (2001, 2004, 2007) to study the *dynamical* passage into equilibrium of initially prolate ($\alpha = \beta$) ellipsoids in pure spin. This may also be relevant to the re-aggregation of asteroids after a disruptive planetary fly-by (cf. Richardson et al. 1998).

4.1   Governing equations

Because we have incorporated a rigid-plastic rheology, the ellipsoid can switch between the rigid and plastic states. When rigid, the ellipsoid simply continues to spin at a fixed rate, as there are no external influences. Thus, it is only necessary to obtain equations for the case when the ellipsoid has failed and is flowing plastically.

Equations governing the dynamics of a plastically flowing, rigid-plastic ellipsoidal asteroid are obtained by evaluating (27) and (28) in the coordinate system aligned with the ellipsoid's principal axes. This coordinate system is assumed to have an angular velocity tensor $\boldsymbol{\Omega}$ that may be different from the spin tensor $\boldsymbol{W}$ of the deforming ellipsoid. Accordingly, due care must be taken while evaluating derivatives of tensors, e.g., $\dot{\boldsymbol{I}}$ and $\dot{\boldsymbol{L}}$. In general, for any tensor $\boldsymbol{B}$, the components of the tensor's rate of change, represented by $[\dot{\boldsymbol{B}}]$, differ

---

[6] This elucidates why the angle of repose is nearly constant for a wide variety of grains.

from the rate of change of $\boldsymbol{B}$'s components, denoted by $\overline{[\dot{\boldsymbol{B}}]}$, when evaluated in a rotating coordinate system. They can be shown to be related to each other by

$$[\dot{\boldsymbol{B}}] = \overline{[\dot{\boldsymbol{B}}]} + [\boldsymbol{\Omega B}] - [\boldsymbol{B\Omega}].$$

Using the above with Eqns. (27) and (28) yields

$$\overline{[\dot{\boldsymbol{L}}]} + [\boldsymbol{\Omega L}] - [\boldsymbol{L\Omega}] + [\boldsymbol{L}]^2 = -[\boldsymbol{A}] - (\alpha\beta)^{2/3}[\overline{\boldsymbol{\sigma}}\,\boldsymbol{Q}^{-1}] \tag{41}$$

and

$$\overline{[\dot{\boldsymbol{Q}}]} + [\boldsymbol{\Omega Q}] - [\boldsymbol{Q\Omega}] = \frac{2}{3}\alpha\beta(\alpha + \beta)[\boldsymbol{Q}] + [\boldsymbol{LQ}] + [\boldsymbol{QL}^T], \tag{42}$$

where, as before, the square brackets signify evaluation of a tensor in the principal-axes coordinate system.

We proceed by decomposing $\boldsymbol{L}$ in (41) into its symmetric and anti-symmetric parts $\boldsymbol{D}$ and $\boldsymbol{W}$, and taking the symmetric and anti-symmetric parts of the resulting equation. We obtain

$$\overline{[\dot{\boldsymbol{D}}]} + [\boldsymbol{\Omega D}] - [\boldsymbol{D\Omega}] + [\boldsymbol{D}]^2 + [\boldsymbol{W}]^2 = -[\boldsymbol{A}] - (\alpha\beta)^{2/3}\frac{1}{2}\left([\boldsymbol{\sigma}\,\boldsymbol{Q}^{-1}] + [\boldsymbol{Q}^{-1}\boldsymbol{\sigma}]\right)$$

and

$$\overline{[\dot{\boldsymbol{W}}]} + [\boldsymbol{\Omega\,W}] - [\boldsymbol{W\Omega}] + [\boldsymbol{D\,W}] + [\boldsymbol{W\,D}] = -(\alpha\beta)^{2/3}\frac{1}{2}\left([\boldsymbol{\sigma}\,\boldsymbol{Q}^{-1}] - [\boldsymbol{Q}^{-1}\boldsymbol{\sigma}]\right).$$

Finally, we substitute for the stress from (26) into the above equations, as the ellipsoid is supposed to be in a plastic state, and employ the forms that the various tensors take in the principal-axes coordinate system, as outlined in Sec. 2.3. This yields the following set of equations for the components of $\boldsymbol{D}$ and $\boldsymbol{W}$

$$\dot{D}_1 - 2D_{12}\Omega_3 + D_1^2 + D_{12}^2 - W_3^2 = -A_1 - p\,(\alpha\beta)^{2/3}\left(k\frac{D_1}{|\boldsymbol{D}|} - 1\right), \tag{43}$$

$$\dot{D}_2 + 2D_{12}\Omega_3 + D_2^2 + D_{12}^2 - W_3^2 = -A_2 - p\frac{(\alpha\beta)^{2/3}}{\alpha^2}\left(k\frac{D_2}{|\boldsymbol{D}|} - 1\right), \tag{44}$$

$$\dot{D}_3 + D_3^2 = -A_3 - p\frac{(\alpha\beta)^{2/3}}{\beta^2}\left(k\frac{D_3}{|\boldsymbol{D}|} - 1\right), \tag{45}$$

$$\dot{D}_{12} + (D_1 - D_2)\Omega_3 - D_3 D_{12} = -p\,(\alpha\beta)^{2/3}\,k\frac{D_{12}}{|\boldsymbol{D}|}\frac{1}{2}\left(1 + \frac{1}{\alpha^2}\right) \tag{46}$$

and

$$\dot{W}_3 - D_3 W_3 = -p\,(\alpha\beta)^{2/3}\,k\frac{D_{12}}{|\boldsymbol{D}|}\frac{1}{2}\left(1 - \frac{1}{\alpha^2}\right), \tag{47}$$

where

$$|\boldsymbol{D}| = \sqrt{D_1^2 + D_2^2 + D_3^2 + 2D_{12}^2}, \tag{48}$$

follows from the definition of $|\boldsymbol{D}|$. In order to determine the pressure p, we use the fact that, because volume is conserved during plastic flow, tr $\boldsymbol{D} = D_1 + D_2 + D_3$ vanishes for all time. Thus, $\dot{D}_1 + \dot{D}_2 + \dot{D}_3 = 0$ and Eqns. (43) - (45) are not independent, and adding these three equations together yields

$$p = -\frac{(\alpha\beta)^{-2/3}\,(2 + |\boldsymbol{D}|^2 - |\boldsymbol{W}|^2)}{k\,\mathrm{tr}\,(\boldsymbol{D}\boldsymbol{Q}^{-1})/|\boldsymbol{D}| - \mathrm{tr}\,\boldsymbol{Q}^{-1}}, \qquad (49)$$

where we have employed the relation $A_1 + A_2 + A_3 = 2$ quoted previously in Sec. 2.4.

Turning now to (42), we again set $\boldsymbol{L} = \boldsymbol{D} + \boldsymbol{W}$, and employ the forms of $\boldsymbol{Q}$, $\boldsymbol{D}$ and $\boldsymbol{W}$ given in Secs. 2.2 and 2.3, to obtain, after simplification,

$$\dot{\alpha} = (D_2 - D_1)\alpha, \qquad (50)$$
$$\dot{\beta} = (D_3 - D_1)\beta \qquad (51)$$

and

$$\Omega_3 = W_3 + \frac{1 + \alpha^2}{1 - \alpha^2} D_{12}. \qquad (52)$$

While the first two equations keep track of the shape via the axes ratios, the last equation relates the rotation rate of the principal-axes coordinate system Ω_3 to the spin rate W_3. Note that the two rates differ by the presence of a shear flow in the equatorial plane. In statics, the shear flow vanishes and the two rates Ω_3 and W_3 coincide.

Eqns. (43), (45), (46) - (52) form a closed system of equations describing the motion of a rigid-plastic, spinning triaxial ellipsoid in its plastic state. Unfortunately these equations, though simple [7], are still not amenable to a closed-form solution, and we must resort to numerical integration, taking care to track the material switching back and forth between rigid and plastic states.

4.2 Switching states

When integrating the volume-averaged equations of motion, one has to follow how the material transitions, or switches, between rigid and plastic states. The criteria we impose to follow these material changes is based on rational plasticity theory (see, e.g., Simo and Hughes 1997), and was outlined in detail in Sec. 2.1. In summary, the body ceases to be rigid once the yield condition is violated. In our case, this is the Drucker-Prager yield criterion of (19). However, material continues to flow plastically until first the strain rate $\boldsymbol{D}$ drops

---

[7] Simple, at least when compared with the non-linear elliptic PDEs governing elasto-plasto-dynamics!

to zero, and then the material's stress state moves inside the yield surface. This movement of the stress state can only be verified iteratively. When the strain rate vanishes, average stresses are computed assuming rigidity. If these stresses do not violate the yield criterion, the body has indeed transitioned to a rigid state. If not, then, as stated in Sec. 2.1, the material remains in a neutrally loaded plastic state.

At this juncture, it is important to insert a cautionary note. The equilibrium surfaces derived in Sec. 3 should *not* be confused with the material's yield surface. Material in a body cannot continue to remain plastic if the stress state drops below the yield surface, which may occur if the strain rate vanishes. In contrast, a body that is plastically yielding may well come to rest *inside* the equilibrium region corresponding to its internal friction angle, i.e., this body will not freeze into a rigid object the instant its spin and shape parameters pass through either of the two bounding surfaces obtained in Sec. 3. Due to inertia, the body spin-shape state penetrates further into the equilibrium region. This process continues until the material's strain rate goes to zero, thereby preparing grounds for a possible transition to a rigid state. Obviously, the strain rate cannot become zero outside the equilibrium region.

Finally, we mention that the description above of the material's transition has direct analogy with a Coulomb slider - a very accessible one-dimensional frictional model - which is explored in great detail in the first chapter of Simo and Hughes (1997).

4.3 Numerical algorithm

The governing equations developed in Sec. 4.1 are ordinary differential equations that are integrated employing MATLAB's adaptive fourth-order Runge-Kutta solver "ode45". Relative and absolute tolerances were set to 10^{-5} and 10^{-8}, respectively. Attention needs to be paid to the fact that during time integration, the material may switch between rigid and plastic states. To this end, we enforce the following rules at each time integration step.

Rule 1. At the *initial* time, the magnitude of the stretching rate tensor $|\boldsymbol{D}|$ is assumed to be zero. According to the theory developed for rigid-plastic transitions, it is thus possible for the body to be rigid at the beginning.

Once initial conditions for W_3 and β have been specified, we check whether the average rigid stresses provided by (29) violate the yield condition (19). If they do, we step forward in time according to Rule 3, otherwise we follow Rule 2 when incrementing time. Depending on whether the yield condition is violated or not,

we designate the body to be rigid or yielded at the end of this step.

Rule 2. If the body at the end of the previous time integration step was rigid, we simply keep checking the yield condition at every subsequent time increment. If, and when it is violated, the body is designated to have yielded, and we switch to Rule 3 of the algorithm. If it is not violated, the body continues to be rigid and we step forward in time according to the present Rule.

Rule 3. If the body at the end of the previous integration step had yielded, we compute its dynamics according to the equations outlined in Sec. 4.1. As the body deforms plastically, it changes shape and so its rotation rate adjusts accordingly to conserve angular momentum. During this process, it is possible for the body to switch back to a rigid state. To this end, we continuously monitor the magnitude of the stretching rate tensor $|\boldsymbol{D}|$. If it vanishes, we invoke Rule 4, else the body continues to flow plastically and we maintain the present Rule.

Numerically checking when $\boldsymbol{D}$ is zero is simple enough in one dimension, as zero crossings are easy to identify. In higher dimensions, though, we have the option of either trying to locate the simultaneous zero crossings of each component of $\boldsymbol{D}$, or trying to find when the algebraic function $|\boldsymbol{D}|$ becomes zero. The latter option is simpler, though caution must be exercised, as $|\boldsymbol{D}|$ is always positive, so that it does not cross the zero plane; instead it just touches that surface. To detect the zero crossings of $|\boldsymbol{D}|$, we employ the "events" function in MATLAB along with an allowable error of 10^{-6}.

Rule 4. Because $|\boldsymbol{D}| = 0$, there is a possibility that the body can transition back to a rigid state. So, we assume that the body is rigid, calculate the (average) rigid stresses from (29), and check whether the yield condition (19) is violated or not. If it is, then the body persists in a plastic, but neutrally loaded state. We thus designate the body as yielded and return to Rule 3. Conversely, if the yield condition is satisfied, the body is said to be rigid and we go back to following Rule 2.

To check the accuracy of the numerical integration, we confirmed that the angular momentum, which should be a constant throughout our isolated body's evolution, indeed remains unchanged within tolerance limits. On the other hand, because the body dissipates energy internally during plastic flow, the total energy of the system decreases with time. Plots for both these quantities corresponding to the investigation of Sec. 4.6 are shown in Figs. 15 and 16. The scripts for all routines may be obtained from the first author.

We next investigate the particular case of passage into equilibrium of prolate ellipsoids in pure spin with friction angle $\phi_F = 40^o$.

Richardson et al. (2005) consider equilibrium shapes of spinning ellipsoidal granular aggregates, which they model as a collection of smooth spheres held together by gravity alone. To facilitate a continuum description, we model such an aggregate as a rigid-plastic material with an appropriate yield criterion, as outlined in Sec. 2.1. Typically, granular aggregates dilate when sheared. However, we neglect this aspect of their behavior by assuming a flow rule that preserves volume during plastic flow. But we should emphasize that this is merely a simplifying, and not necessarily limiting, hypothesis. Dilatation may be incorporated in a straightforward manner. We do not do so because it is not obvious whether dilatation is a crucial component in the dynamics investigated here. In fact, in spite of neglecting dilatation, we do achieve below a close match with the results of Richardson et al. (2005). Moreover, because little is known about the bulk modulus of asteroids, the additional complication introduced by addressing compressibility is to be avoided. Whether the spinning dynamics of granular asteroids critically depends on compressibility, remains a question for further research.

Richardson et al. (2005) show that the equilibrium shapes attained by an initially prolate aggregate all reside in a region well approximated by that where *prolate* rigid-plastic ellipsoids obeying a Mohr-Coulomb yield criterion with a friction angle $\phi_F = 40^o$ could exist in equilibrium. Note, however, that the final shapes that they obtain were themselves *not* prolate, but triaxial. To compare our approach with theirs, we first investigate the passage into equilibrium of spinning rigid-plastic prolate ellipsoids folowing a Drucker-Prager yield criterion with $\phi_F = 40^o$ for various initial values of the axes ratios $\alpha = \beta$. Our selection of ϕ_F was motivated by the choice of Richardson et al. (2005), and we comment upon its suitability in the next section. For the moment we proceed to discuss the results for the $\phi_F = 40^o$ case that are displayed in Fig. 8.

The average pressure is often enforced to be compressive (positive) in non-cohesive granular materials, and is supposed to capture our anticipation that such aggregates will disintegrate (lose coherence) when the average pressure becomes tensile (negative). This is similar, but less stringent, than the requirement for compressive internal stresses that has modeled failure in such materials (i.e., the tensile criterion mentioned in Sec. 2.1) and yields the curve C_1 in Fig. 8. We expect any rubble pile with initial conditions that place it above this curve to disrupt due to its inability to sustain negative pressures, and so we call the curve C_1 the *disruption* curve. It is possible that the object coalesces post-disruption, but that process cannot be studied under the present plasticity model and would require employing a description suitable for loose granular aggregates, as is done in Sharma et al. (2006). The curve C_2

is the upper critical curve predicted by the smooth Drucker-Prager criterion for a friction angle of 40°. Any *prolate* ellipsoid (with $\phi_F = 40^o$) that lies below this curve will exist in equilibrium. Also shown in Fig. 8 is the critical curve C_3 obtained from the Drucker-Prager criterion that bounds from below the region of possible equilibrium shapes. Both C_2 and C_3 are precisely the upper and lower bounding curves corresponding to $\phi_F = 40^o$ in Fig. 6.

We proceed to investigate the evolution of the rotation rate Ω_3 with the changing axes ratios α and β. Note that we choose to concentrate on Ω_3 rather than the spin rate W_3. The reason lies in the fact that the former quantity can in fact be observed in an experiment, as it measures the change in the ellipsoid's principal axes. The rate W_3, being a local variable, is not that easily available, though it may be estimated from (52). Recall that both these rates coincide once deformation ceases.

Figure 8 plots the evolution of the rotation rate Ω_3 of the ellipsoid's principal axes against the axes ratios β and α. Though the ellipsoid is prolate initially, Figs. 8(a) and 8(b) show that it evolves as, and into, a triaxial object. Ellipsoids are grouped into bodies that begin with the same initial shape, but five different initial spins (five symbols atop one another at the same β or α), with each group having its own unique symbol. The initial and ultimate positions are connected by the actual evolution path. We note that several of these paths curve up just before reaching a final state; this occurs because we are plotting the rotation rate Ω_3. Recall that Ω_3 may be different from the actual rate W_3 at which the object's material points rotate owing to the presence of shear strains. Due to inertia, the shear flow retards the angular velocity of the principal axes (see Eqn. (52)), so that Ω_3 is smaller than the spin W_3 (cf., Fig. 14, $\phi_F = 30^o$ curve). As the asteroid equilibrates, the shear rate drops to zero (cf., Fig. 11, $\phi_F = 30^o$ curve) and the rate Ω_3 now increases to coincide with W_3. We explore the homogeneous rotational dynamics of a spinning deformable ellipsoid in much more detail in the next section.

In contrast to the ellipsoids above the disruption curve C_1, ellipsoids with initial conditions between C_1 and C_2 start with positive (compressive) average pressures. Thus, it is expected that these bodies will deform dynamically as coherent objects until they reach an equilibrium shape, i.e., the average pressure remains positive throughout the ellipsoid's evolution to a static state. This is, in fact, seen to be the case, and so we denote the region between the curves C_1 and C_2 as the *deforming* zone. The final equilibrium shape, *if* prolate, must necessarily lie between the failure curves C_2 and C_3. Fig. 8 shows the results with the initial and final states connected. Because the final shape is often triaxial, some final states may lie above the curve C_2, as seen in a few cases of Fig. 8(a). These states will, however, lie below the corresponding bounding curve for a triaxial ellipsoid with the appropriate axes ratios.

36
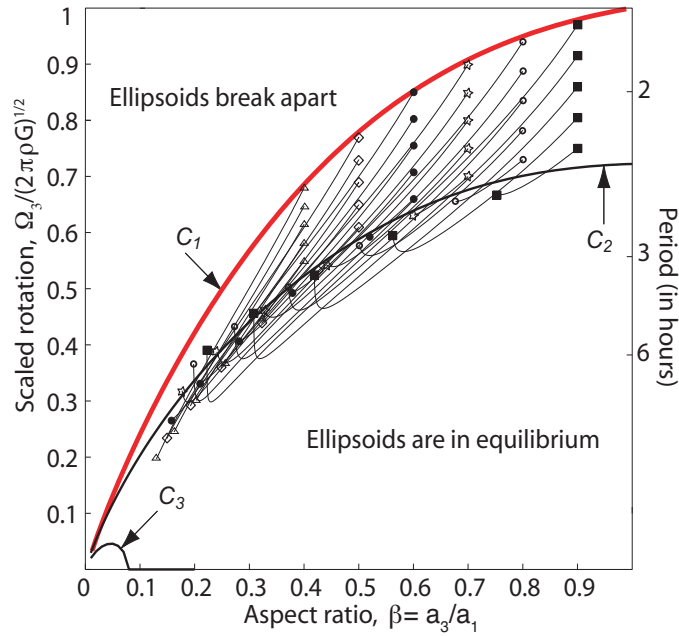
(a) The evolution of the rotation rate versus the axes ratio β.
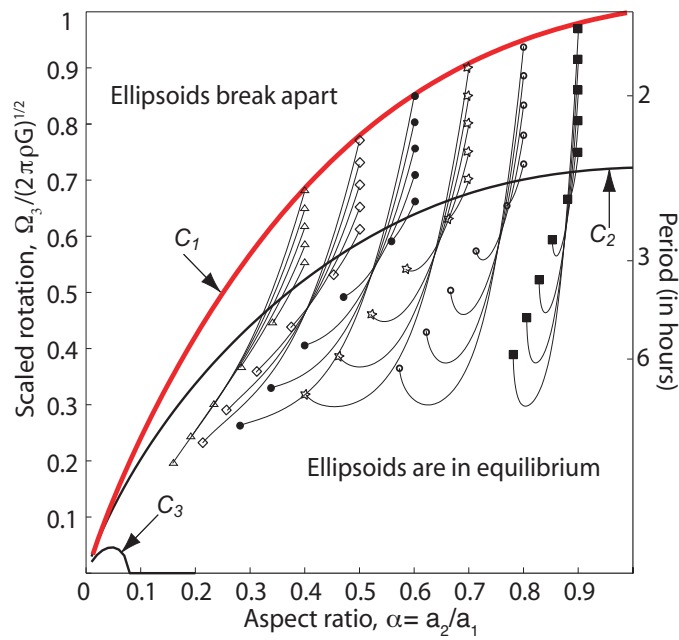
(b) The evolution of the rotation rate versus the axes ratio α.

Fig. 8. Passage into equilibrium of initially prolate ellipsoids. The curves C_i are described in the text. The symbols signify groups of test ellipsoids that are initially prolate, and lie between C_1 and C_2. The lines follow the deformation of each group until their final states that are marked by the same symbol.

37

Richardson et al. (2005) classify their ellipsoids into objects that, while equilibrating, retain all of their mass, ones that lose 10% of their mass and those that lose more than 10% mass; these are marked by green, yellow and red symbols, respectively, in their Fig. 2. Unlike Richardson et al. (2005), while we can predict a disruption by observing an object's elongation, we cannot follow its entire evolution. Our ellipsoids are restricted by our kinematic assumption to deform into another, possibly very elongated, ellipsoid; however, in reality, under such conditions we expect the body to start necking. This may, perhaps, be addressed by using higher-order moments. Keeping in mind these constraints, we identify objects whose internal pressures become tensile (negative) with objects reported by Richardson et al. (2005) to lose more than 10% of their mass (their 'red objects'), while objects losing none, or less than 10%, of their mass (their 'green and yellow objects') are associated with ellipsoids that originate inside the curve C_1 in Fig. 8.

Richardson et al. (2005) report that objects that begin within the curve C_2 remain essentially unchanged, just as our theory would predict. These bodies are not marked in Fig. 8. Ellipsoids that are seen by Richardson et al. (2005) to lose more than 10% of their mass appear to be born in a region that is well approximated by the *disruption* zone lying beyond the curve C_1, lending substance to our earlier identification of C_1 as a disruption curve. Finally, comparing ellipsoids that initiate between curves C_1 and C_2 in Fig. 8 with those of Richardson et al. (2005) that deform and lose less than 10% of their mass, if at all, we find that there is a qualitative and, in some respects even quantitative, match. Richardson et al. (2005) note that such objects originate from a rather narrow section above the curve C_2, akin to the deforming zone between the failure curve C_2 and the disruption curve C_1; in this band, ellipsoids elongate as they equilibrate.

4.5   Comment: Internal friction and overall deformation

In this section, we put forth a couple of unsettled issues that need to be resolved in order to bring both our continuum model, and the N-body simulations of Richardson et al. (2005), closer to reality. In both cases, several avenues of future exploration suggest themselves as possible explanations.

Richardson et al. (2005) found that critical curves of a Mohr-Coulomb material with an internal friction angle ϕ_F of 40° constrained their equilibrated, approximately-prolate rubble piles. This high value for ϕ_F is worrisome. Most dry cohesionless granular materials, like sand, tend to have friction angles around 30°; 40° is seldom observed. Our observation in Sec. 3 that the equilibrium surfaces obtained from an application of the Drucker-Prager yield criterion contain the surfaces derived from a Mohr-Coulomb criterion offers
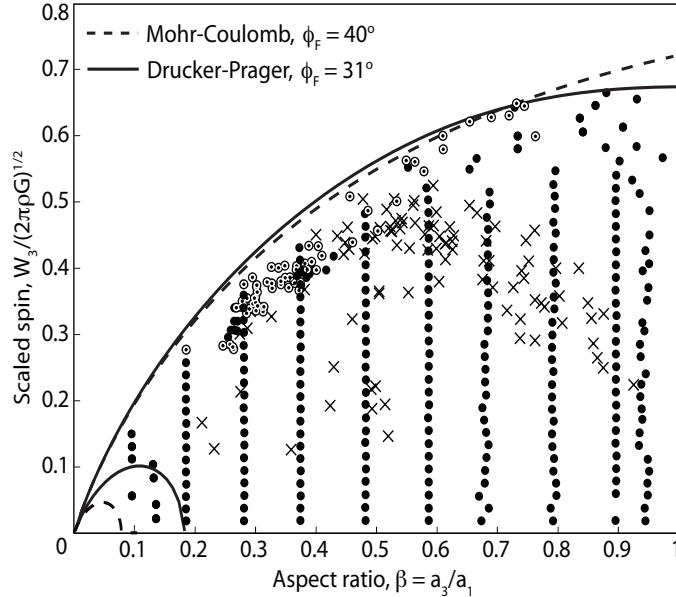
Fig. 9. Final locations in spin-shape space of all rubble piles tested by Richardson et al. (2005). The filled circles, ringed dots and the crosses correspond to the green (no mass loss), yellow (less than 10% mass loss) and red symbols (more than 10% mass loss) in Fig. 2 of Richardson et al. (2005), respectively.

a possible solution. Indeed, Fig. 9 shows that the 31° Drucker-Prager curve, provides a perfectly adequate upper bound to the data of Richardson et al. (2005). A friction angle of 31° is, of course, much more satisfying, and this explanation suggests that gravitating rubble piles may be better modeled as Drucker-Prager materials rather than Mohr-Coulomb ones. The fact that the lower Drucker-Prager bound does not constrain a few ellipsoids with axes ratio $\alpha \approx \beta \approx 0.1$ should not cause anxiety. At their current resolution, a prolate rubble pile of Richardson et al. (2005) with axes ratio $\beta \approx 0.1$ has a mere two to three spheres lining its short axes. At this coarse resolution there is little reason to expect a close match between a continuum theory and a discrete simulation. Thus, it is perhaps more appropriate to concentrate on bounding the equilibrium shapes of Richardson et al. (2005) from above.

Other factors may influence the internal friction. First, it is possible that the internal friction angle be high in N-body simulations of identical frictionless spheres due to the spheres arranging themselves into regions of periodic packing. Indeed, Richardson et al. (2005) assemble their rubble piles initially in a hexagonal closed packing (see their Sec. 2.1). This may be verified, and subsequently corrected, by introducing a small amount of poly-dispersity in the rubble piles. Second, an asteroids constituent material characterized with an internal friction angle of, say, 31°, is expected to form a cone of this same angle when poured into a pile on Earth. However, granular matter on the Earth experiences a uniform vertical gravitational attraction. In the case of rubble piles in space, this gravitational force is radial. It is not obvious whether we

can disregard the effects of a changed gravitational field on our continuum interpretations of the results of Richardson et al. (2005), and this too remains a problem for further scrutiny.

Another issue is that, on average, in the analysis of Sec. 4.4 we observe less deformation than do Richardson et al. (2005). Again there are several possible explanations. An immediate one being that because we allow our ellipsoids to only deform into ellipsoids, we are truncating deformation modes like necking that may enhance deformation. This could also be attributed to our use of the critical curve C_2 that corresponds to the high friction angle of 40° as the upper boundary of the equilibrium region. As discussed above, there is good reason to believe that only a friction angle of 31° may suffice. Because the critical curve for a material with a ϕ_F of 31° lies below C_2 that is due to a higher friction angle, utilizing the former curve delays transition to rigidity, thereby enhancing deformation. Finally, we may be observing less deformation because in the model of Richardson et al. (2005), the internal friction's origin is geometric alone, i.e., due to the aggregate's packing, as the constituent spheres are smooth (see also the discussion in Sec. 3.6). Thus, in their case, the frictional resistance contributes at higher packing fractions, reducing in magnitude as the aggregate becomes mobile and begins to deform. In contrast, our model preserves volume, and does not differentiate between geometric and surface friction, leading to a greater overall frictional effect, causing the ellipsoid to reach equilibrium more quickly. This could be amended by using a flow rule that is not volume-preserving and, further, by allowing the friction to depend on the packing fraction to simulate a geometric dependency. Alternatively, we could model the aggregate at lower packing fractions as a dense gas of smooth spheres, whose rheology transitions to that of a rigid-plastic material as the aggregate condenses, somewhat along the lines of Sharma et al. (2006).

4.6 Discussion: Dynamics of a homogeneously deforming ellipsoid

In this section, we describe in detail the dynamics of a rigid-plastic spinning ellipsoid, beginning with fixed initial axes ratios, but exploring the response for several values of the internal friction. We find that our extremely simplified model exhibits dynamical behavior that is likely to be relevant to the relaxation and rearrangement of rubble asteroids after, for example, a planetary fly-by, or in failure situations where the "centrifugal" forces due to spin override external effects like tidal stresses.

Figures 10 - 13 display the histories of the shapes, strain rates and angular velocities for a rigid-plastic ellipsoid with initial axes ratios $\alpha = \beta = 0.7$, and an initial non-dimensional angular velocity $\Omega_3(0) = W_3(0) = 0.695$, which corresponds to a rotation every 2.74 hours for a body of density 2 g/cm^3. The

strain rates are assumed to be zero at the start of the integration. Our choice of initial spin is such that ellipsoids with internal friction angles $\phi_F \lesssim 30^o$ will fail, allowing interesting dynamics to occur; see Fig. 6.

We observe that a majority of spinning ellipsoids elongate into cigar-shaped objects ($\alpha \approx \beta \ll 1$), as indicated by the lowered values of the axes ratios α and β in Fig. 10. A number of asteroids are known to have such elongated shapes, e.g., 25143 Itokawa, 4179 Toutatis, etc. From Fig. 10, we see that the axis ratios α and β have alternately large and small oscillations. This variation occurs because volume is conserved, so that the strain rates obey $D_1 + D_2 + D_3 = 0$, and Eqns. (50) and (51) that govern the axes ratios' evolution are coupled to Eqns. (43) - (46) that control the strain rates. The increase in β's amplitude is not surprising if we consider the inviscid case, where, without energy dissipation, oscillations never damp out. In fact, if the axes ratios α and β are followed for longer times, their histories consist of small and large amplitude motions. Thus, though the ratio α appears to damp out in the frictionless case in Fig. 10(a), it actually does not, with its amplitude growing again later. At low friction angles, the behaviors of the parameters α and β are similar, except that the oscillations do eventually die out.

We saw above that once the body fails, it begins to elongate, as indicated by the initially negative strain rate D_3 in Fig. 12(a), and the initially positive strain rate D_1 in Fig. 12(b). But, because this elongation increases the moment of inertia around the spin axis, conservation of angular momentum requires the spin to decrease. As the spin decreases, "centrifugal" stresses begin to drop relative to the gravitational stresses, and the strain rates D_3 and D_1 lessen in magnitude. A decrease in the spin W_3 tends to move the state of the body down into a region where it can exist in static equilibrium, as suggested by, say, Fig. 4 in Holsapple (2001). But, recall from a previous discussion that a plastically flowing body cannot suddenly stop, owing to the inertia of each plastically flowing element. If $|\boldsymbol{D}|$ reaches zero while inside this region, the body halts, and this is observed to occur for higher friction angles $\phi_F \sim 20^o - 30^o$.

On the other hand, for lower friction angles, it is possible for the body to actually cross the lower bound of this region of possible equilibrium solutions. This is apparent, for example, on curves corresponding to a friction angle $\phi_F = 5^o$. After a while, however, the gravitational stresses dominate the "centrifugal" stresses and the body starts collapsing. This is marked by an increase in α and β, and a positive D_3. Again, angular momentum conservation causes the body to spin up, thus increasing the "centrifugal" stresses. This spin increase causes the body's state to once again enter the region of equilibrium solutions, where it can stop if $|\boldsymbol{D}|$ becomes zero while it lies within this region. This is observed to occur, for example, in cases with $10^o < \phi_F < 15^o$. If this does not happen, the body crosses the upper failure curve, and is back in a state similar to its initial one; then the whole process restarts, albeit with its spin reduced
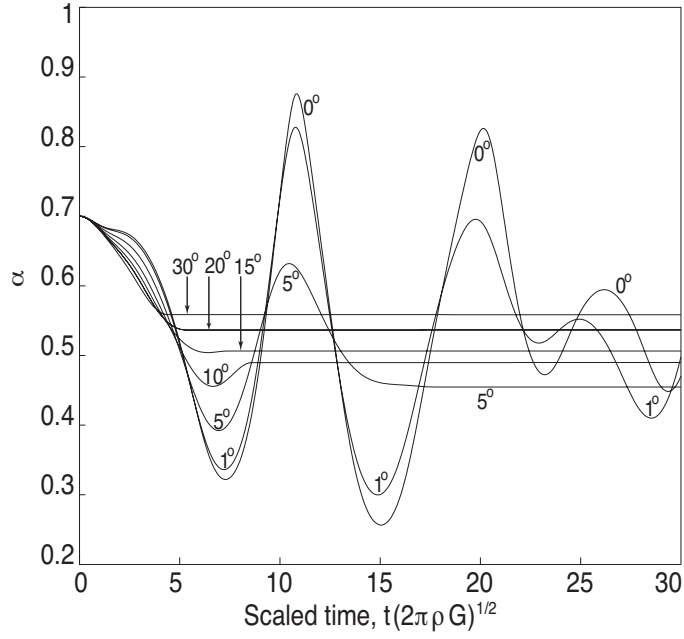
(a) $\alpha = a_2/a_1$
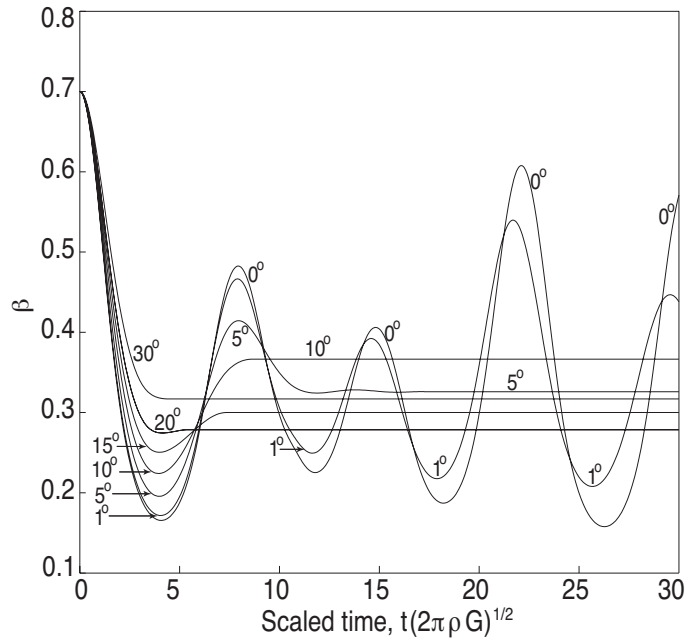
(b) $\beta = a_3/a_1$

Fig. 10. Time evolution of the axis ratios α and β for different values of the friction angle. ϕ_F listed on curves. These histories correspond to an initially prolate asteroid with axes ratios of 0.7 and a spin of 2.74 rotations per hr for $\rho = 2$ g cm^{-3}.
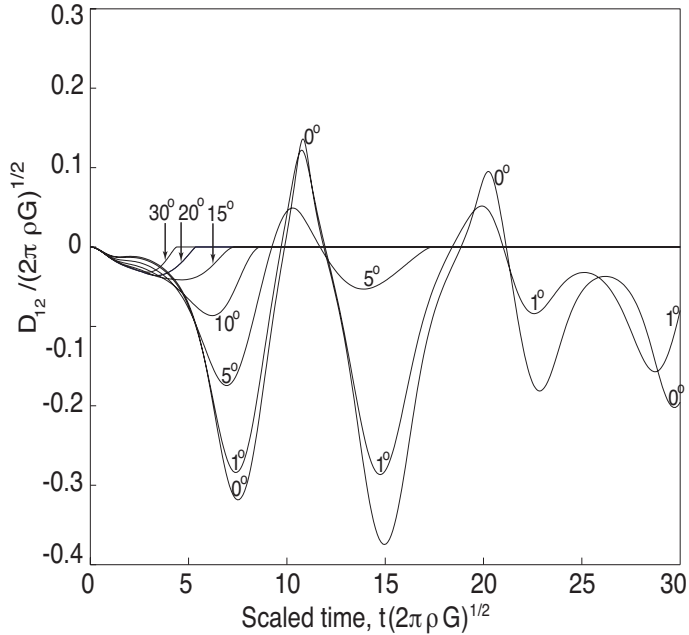
42

Fig. 11. The evolution of the scaled shear-strain rate D_{12} for different values of the friction angle. See also Fig. 10's caption.

owing to the effects of internal friction. Note that this entails that the ellipsoid necessarily deforms in a manner that increases its rotational inertia, so that angular momentum remains conserved. Finally, as seen for $\phi_F = 1^o$, 5° and 10°, the body can execute several oscillations before becoming rigid.

A major difference from symmetrical ellipsoids is the presence of the shear flow D_{12} shown in Fig. 11. Note that the amount of shearing strain rate D_{12} increases with decreasing friction. In general, oscillations in the various quantities show an increase with decreasing friction, as is to be expected. Another aspect in which a prolate ellipsoid differs from an oblate one is in the presence of a "slip" angular velocity shown in Fig. 14. This is the difference between the angular velocities Ω_3 of the ellipsoid's principal coordinate-system (Fig. 13(a)) and the spin angular velocity W_3 associated with the spin tensor $\boldsymbol{W}$ (Fig. 13(b)). Alternatively, the former (Ω_3) can be thought of as a macroscopic rotation rate that can be seen in an observation of the bulk motion of the ellipsoid, while the latter (W_3) is a microscopic spin rate that measures the pace at which an infinitesimal material volume inside the ellipsoid turns. Note that the slip angular velocity goes to zero when the ellipsoid passes into a rigid state. Such a situation will occur only when there is non-zero friction. Thus, the slip rate of an inviscid fluid ellipsoid will never decay to zero. For all cases, the initial slip rate is negative, corresponding to the shear rate D_{12} being initially negative, which is plausible, because when the ellipsoid starts to flow plastically, the longest axis tends to increase at a faster rate, as "centrifugal" effects increase with distance while gravitational effects decrease. This means that $D_1 > D_2$ initially. When this is coupled to a counter-clockwise rotation,
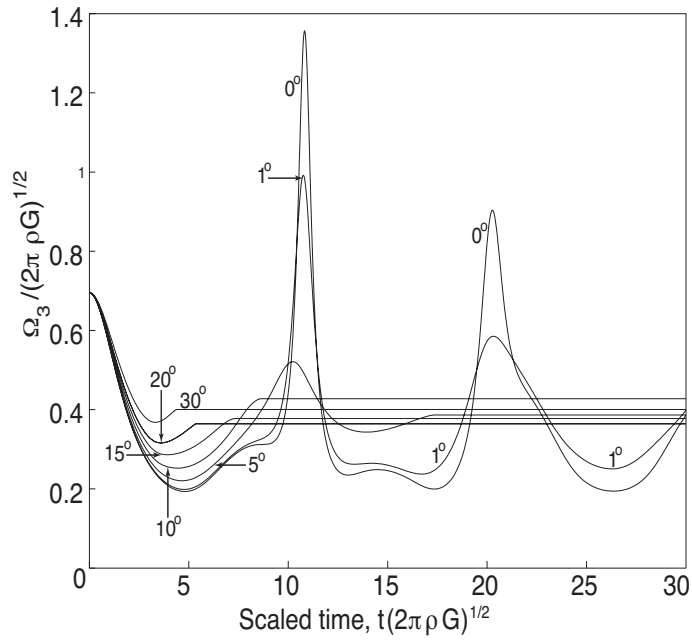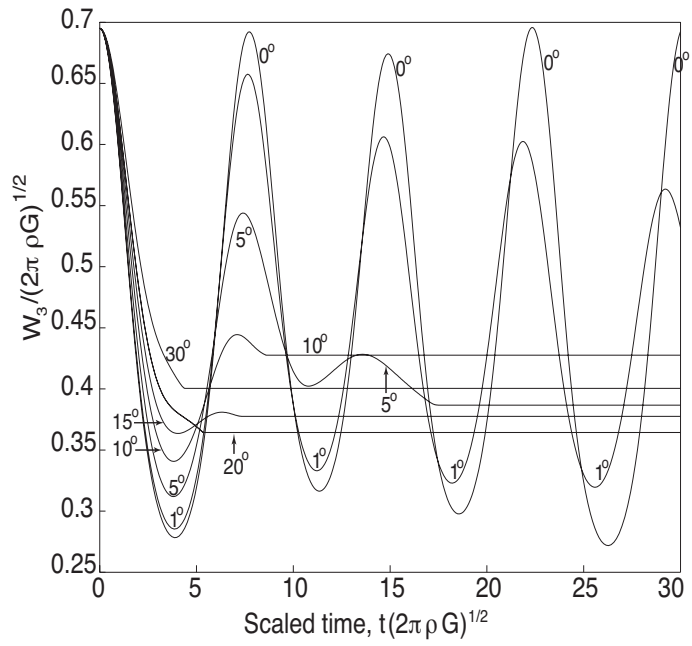
43
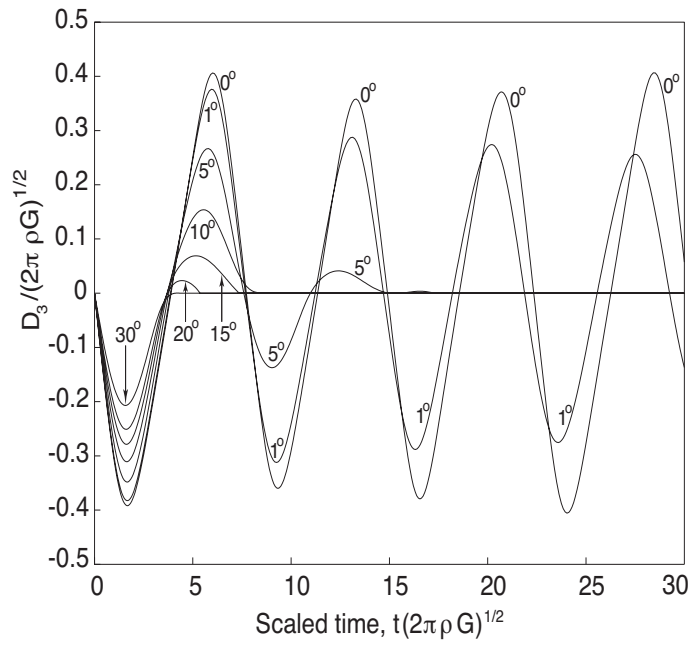
(a) Scaled strain rate D_3
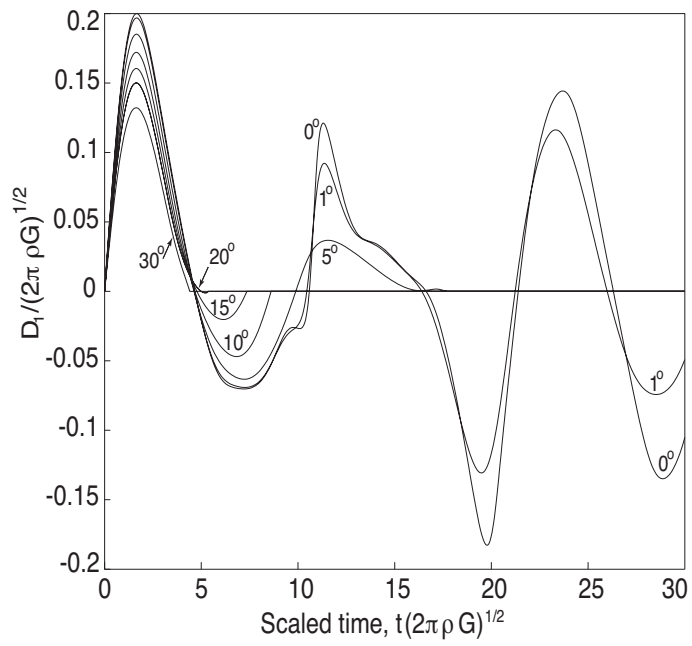
(b) Scaled strain rate D_1

Fig. 12. The evolution of the normal-strain rates D_3 and D_1 for different values of the friction angle. See also Fig. 10's caption.

44

(a) Scaled macroscopic rotation rate Ω_3

(b) Scaled microscopic spin W_3

Fig. 13. The evolution of the angular velocity of the ellipsoid's principal axes (Ω_3) and the rotation rate associated with material deformation (W_3). A number of friction angles are investigated. See also Fig. 10's caption.

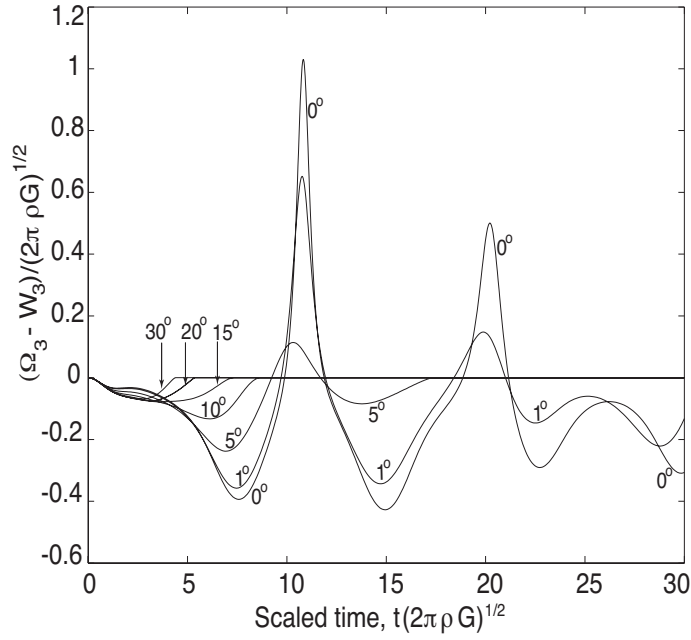Fig. 14. The difference between the angular velocities Ω_3 and W_3 plotted in the previous figure, that is, the "slip". Histories for different values of the friction angle are shown. See also Fig. 10's caption.
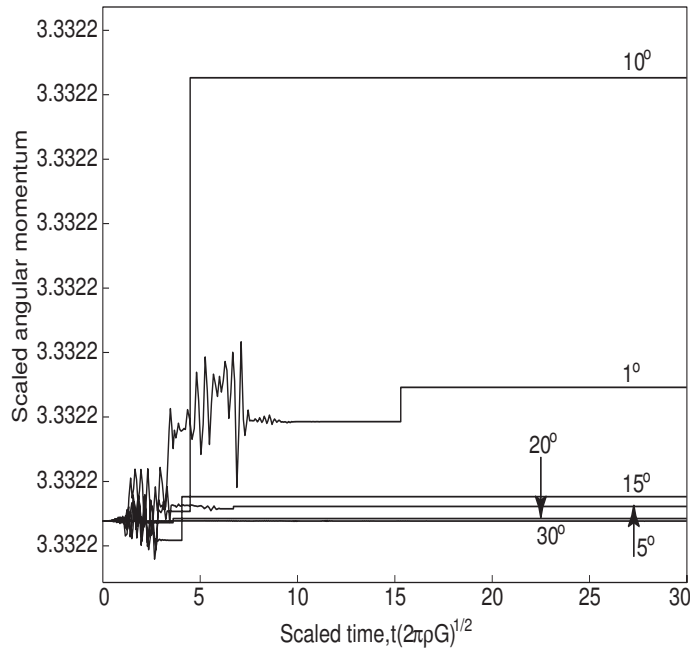

Fig. 15. Angular momentum along the spin axis for several friction angles. In pure spin, this is the only non-zero component. See also Fig. 10's caption.

the angle between the 1 and 2 axes tends to increase, which corresponds to an initially negative shear rate.

Finally, we consider the evolution of the angular momentum and the total
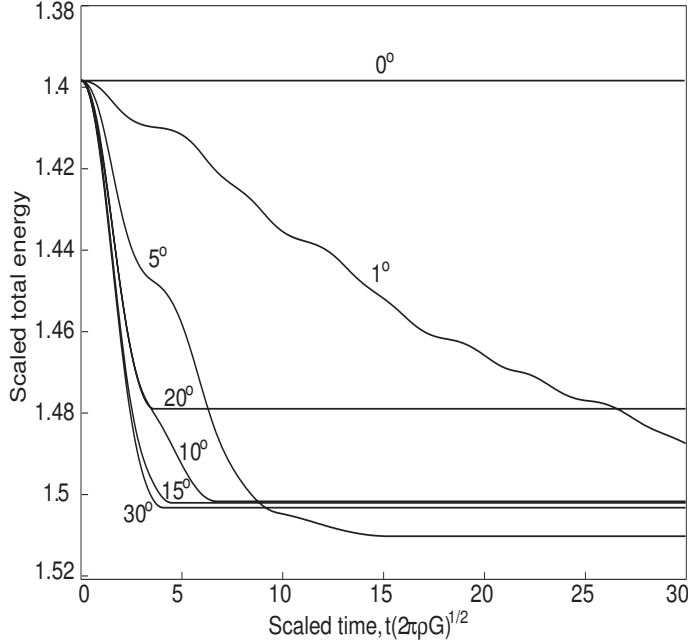
46

Fig. 16. Total energy, which is the sum of gravitational and kinetic energies, for several friction angles. See also Fig. 10's caption.

energy. As remarked at the end of Sec. 4.3, the angular momentum is a constant of the motion. Figure 15 confirms this to be true to at least four decimal places, thereby providing a check on the computations. The total energy of a self-gravitating spinning ellipsoid is composed of both gravitational and kinetic parts. Relevant formulae for their computation are provided in Sharma (2004). There it is also noted that care is required when computing the gravitational potential energy. This is because the spatially invariant part of the gravitational potential, the *gauge*, depends on the body's shape, which changes with time. Thus, this time-varying gauge cannot be utilized set the datum, as is very often done. Instead, we have to retain the gauge term in the gravitational potential for all energy budgets, in spite of the fact that it makes no contribution to the internal gravity force; the latter being the spatial gradient of the gravitational potential. Here we simply plot the total energy in Fig. 16 for the different friction angles investigated above. As expected, the total energy is a constant for an inviscid fluid ($\phi_F = 0^o$) and decreases when $\phi_F > 0^o$ due to frictional losses. Once the body becomes rigid, the energy remains constant. The rate of dissipation, measured by the slope of the curves, increases with the friction angle. These checks that are consistent with physical requirements provide further confirmation of our numerics. There is an interesting aspect to the plot of the total energy, however: as we vary the friction angle, the total amount of energy dissipated, does not increase (or decrease) monotonically with increasing friction. This may seem contradictory, as more frictional materials are anticipated to dissipate greater energy. However, this is only true if the total strain is the same, which is not the case here. Indeed, there is no ordering in the final values of the axes ratios α and β in Fig. 10. This as-

47

pect is in fact a feature of dry-frictional materials; materials whose behavior, as the rate-independent stress response (26) during plastic flow suggests, our rigid-perfectly-plastic object imitates.

The above examples illustrate that, although we model the dynamics of a spinning rigid-plastic ellipsoid in an extremely simple manner, the resulting motion of the ellipsoid is physically plausible. The present formulation may be employed to study disruptive tidal encounters of rubble pile asteroids, in cases when the primary mechanism responsible for an asteroid's deformation is its increase in spin due to tidal torques. Formulae are available (Scheeres et al. 2000, 2005) that allow one to estimate the increment in a *rigid* asteroid's spin. As we saw in this section, if a rubble pile's rotation rate is elevated beyond the equilibrium region associated with its internal friction, it will fail, deform, and then ultimately equilibrate into a different shape and rotation state. In a future publication, we plan to employ our relatively simple description of an asteroid's deformational dynamics, in order to relate the spin at which failure is initiated to its final state.

5   Conclusions

We employ a simple, transparent and *unified* method to characterize the equilibrium shapes, and passage into such states, of ellipsoidal asteroids with interiors modeled as cohesionless, rigid-perfectly-plastic materials following a Drucker-Prager yield criterion. This approach was previously used to study the disruption of asteroids during planetary fly-bys (Sharma et al. 2006), in which case the results agreed well with earlier numerical simulations (e.g., Richardson et al. 1998). We saw that employing a Drucker-Prager yield criterion allowed us to match the equilibrium data of Richardson et al. (2005) to a material with an internal friction angle of 31°, a much more satisfactory value than the earlier Mohr-Coulomb estimate of 40°. We also demonstrated that our *dynamical* approach collapses to an analogous version followed by Holsapple (2007) in the special case of *statics*, and this gave us confidence to apply it to the more complicated situation of passage into equilibrium. The fact that we recover Holsapple's (2007) results exactly, and those of Richardson et al. (2005) approximately, has a number of implications for the present approach. First, it can be employed to explore the non-equilibrium dynamics of rigid-plastic ellipsoids in a rather simple manner, as was done for prolate ellipsoids here, with the added ability of quantifying the results of Richardson et al. (2005). Also, different internal rheologies may be explored. Finally, the volume-averaged approach is amenable to systematic improvements. For example, it is possible to extend the analysis to more general shapes by using higher-order moments, which will also enable one to follow the disruption process more completely. Such an analysis of general shapes will likely be fruitful

considering the multi-varied forms seen amongst asteroids.

6 Acknowledgements

References

Abramowitz, M., and I. A. Stegun 1965. *Handbook of Mathematical Functions.* New York: Dover.

Burns, J. A., and V. S. Safronov 1973. Asteroid nutation angles. *MNRAS* **165**, 403–411.

Chandrasekhar, S. 1969. *Ellipsoidal Figures of Equilibrium.* New Haven, CT: Yale Univ. Press.

Chen, W., and D. Han 1988. *Plasticity for Structural Engineers.* New York: Springer-Verlag.

Chree, C. 1889. Further applications of a new solution of the equations of an isotropic elastic solid, mainly to various cases of rotating bodies. *Quart. J. Math* **23**, 11–33.

Fung, Y. 1965. *Foundations of Solid Mechanics.* Englewood Cliffs, NJ: Prentice-Hall.

Holsapple, K. A. 2001. Equilibrium configurations of solid cohesionless bodies. *Icarus* **154**, 432–448.

Holsapple, K. A. 2002. Rubble pile asteroids: Stability of equilibrium shapes. In *Lunar and Planetary Institute Conference Abstracts*, pp. 1843.

Holsapple, K. A. 2004. Equilibrium figures of spinning bodies with self-gravity. *Icarus* **172**, 272–303.

Holsapple, K. A. 2007. Spin limits of solar system bodies: From the small fast-rotators to 2003 EL61. *Icarus* **187**, 500–509.

Holzapfel, G. 2001. *Nonlinear Solid Mechanics.* New York: John Wiley and Sons.

Jenkins, J. T., and S. B. Savage 1983. Theory for the rapid flow of identical, smooth, nearly elastic spherical particles. *J. Fluid Mech.* **130**, 187–202.

Kaasalainen, M., and 21 others 2004. Photometry and models of eight near-earth asteroids. *Icarus* **167**, 178–196.

Kaasalainen, M., J. Torppa, and J. Piironen 2002. Models of twenty asteroids from photometric data. *Icarus* **159**, 369–395.

Koiter, W. T. 1960. General theorems for elastic-plastic solids. In I. N.

Sneddon and R. Hill (Eds.), *Progress in Solid Mechanics*, Volume 1, pp. 167–221. Amsterdam: North-Holland.

Love, A. 1946. *A Treatise on the Mathematical Theory of Elasticity* (4th ed.). New York: Dover.

Ostro, S. J., R. S. Hudson, L. A. M. Benner, J. D. Giorgini, C. Magri, J. Margot, and M. Nolan 2002. Asteroid radar astronomy. In W. F. Bottke Jr., A. Cellino, P. Paolicchi, and R. P. Binzel (Eds.), *Asteroids III*, pp. 151–168. Tucson, AZ: U. Arizona Press.

Papadopoulos, P. 2001. On a class of higher-order pseudo-rigid bodies. *Math. Mech. Solids* **6**, 631–640.

Pravec, P., A. W. Harris, and T. Michalowski 2002. Asteroid rotations. In W. F. Bottke Jr., A. Cellino, P. Paolicchi, and R. P. Binzel (Eds.), *Asteroids III*, pp. 113–122. Tucson, AZ: U. Arizona Press.

Richardson, D. C., W. F. Bottke Jr., and S. G. Love 1998. Tidal distortion and disruption of earth-crossing asteroids. *Icarus* **134**, 47–76.

Richardson, D. C., P. Elankumaran, and R. E. Sanderson 2005. Numerical experiments with rubble piles: equilibrium shapes and spins. *Icarus* **173**, 349–361.

Richardson, D. C., Z. M. Leinhardt, H. J. Melosh, W. F. Bottke Jr., and E. Asphaug 2002. Gravitational aggregates: Evidence and evolution. In W. F. Bottke Jr., A. Cellino, P. Paolicchi, and R. P. Binzel (Eds.), *Asteroids III*, pp. 501–515. Tucson, AZ: U. Arizona Press.

Scheeres, D. J., L. A. M. Benner, S. J. Ostro, A. Rossi, F. Mazari, and P. Washabaugh 2005. Abrupt alteration of asteroid 2004 MN4's spin state during its 2029 earth flyby. *Icarus* **178**, 281–283.

Scheeres, D. J., S. J. Ostro, R. A. Werner, E. Asphaug, and R. S. Hudson 2000. Effect of gravitational interactions on asteroid spin states. *Icarus* **147**, 106–118.

Sharma, I. 2004. *Rotational Dynamics of Deformable Ellipsoids with Applications to Asteroids*. Ph. D. thesis, Cornell University.

Sharma, I., J. A. Burns, and C.-Y. Hui 2005. Nutational damping times in solids of revolution. *Mon. Not. R. Astron. Soc.* **359**, 79–92.

Sharma, I., J. T. Jenkins, and J. A. Burns 2003. Rotational dynamics of a deformable symmetric ellipsoid. *BAAS* **35**, 1034.

Sharma, I., J. T. Jenkins, and J. A. Burns 2005a. Equilibrium configurations and the Roche limit for spinning ellipsoidal soil-like asteroids. *BAAS* **37**, 643.

Sharma, I., J. T. Jenkins, and J. A. Burns 2005b. Equilibrium shapes of ellipsoidal soil asteroids. In R. García-Rojo, H. J. Hermann, and S. McNamara (Eds.), *Proceedings of the 5th International Conference on Micromechanics of Granular Media*, Volume 1, UK. A. A. Balkema.

Sharma, I., J. T. Jenkins, and J. A. Burns 2006. Tidal encounters of ellipsoidal granular asteroids with planets. *Icarus* **183**, 312–330.

Simo, J., and T. Hughes 1997. *Computational Inelasticity*. New York: Springer-Verlag.

Torppa, J., M. Kaasalainen, T. Michalowski, T. Kwiatkowski, A. Kryszczyn-ska, P. Denchev, and R. Kowalski 2003. Shapes and rotational properties of thirty asteroids from photometric data. *Icarus* **164**, 346–383.

Truesdell, C., and R. A. Toupin 1960. The classical field theories. In S. Flügge (Ed.), *Encyclopedia of Physics Vol. III/I: Principles of classical mechanics and field theory*, pp. 226–793. Berlin: Springer-Verlag.